Feedback Inhibition Enables Theta-Nested Gamma Oscillations and Grid Firing Fields

Please cite this article as: Pastoll, H, Solanka, L, van Rossum, MCW & Nolan, MF 2013, 'Feedback Inhibition Enables Theta-Nested Gamma Oscillations and Grid Firing Fields' *Neuron*, DOI: 10.1016/j.neuron.2012.11.032
This is a PDF file of an unedited manuscript that has been accepted for publication.

Feedback inhibition enables theta-nested gamma oscillations and grid firing fields

Hugh Pastoll [1,2,3], Lukas Solanka [2,3] Mark C.W. van Rossum [2], Matthew F. Nolan [1]

[1] Centre for Integrative Physiology, University of Edinburgh, Hugh Robson Building, Edinburgh, EH8 9XD, United Kingdom

[2] Institute for Adaptive and Neural Computation

[3] Neuroinformatics Doctoral Training Centre, School of Informatics, University of Edinburgh, Edinburgh EH8 9AB, United Kingdom

SUMMARY

Cortical circuits are thought to multiplex firing rate codes with temporal codes that rely on oscillatory network activity, but the circuit mechanisms that combine these coding schemes are unclear. We establish with optogenetic activation of layer II of the medial entorhinal cortex that theta frequency drive to this circuit is sufficient to generate nested gamma frequency oscillations in synaptic activity. These nested gamma oscillations closely resemble activity during spatial exploration, are generated by local feedback inhibition without recurrent excitation, and have clock-like features suitable as reference signals for multiplexing temporal codes within rate coded grid firing fields. In network models deduced from our data, feedback inhibition supports co-existence of theta-nested gamma oscillations with attractor states that generate grid firing fields. These results indicate that grid cells communicate primarily via inhibitory interneurons. This circuit mechanism enables multiplexing of oscillation-based temporal codes with rate coded attractor states.

RUNNING TITLE

Nested gamma oscillations in MEC layer II circuits

HIGHLIGHTS

1. Theta frequency drive is sufficient for entorhinal nested gamma oscillations.
2. Stellate cells in entorhinal layer II communicate indirectly via feedback inhibition.
3. Clock-like gamma oscillations result from coordination of inhibition and excitation.
4. Feedback inhibition multiplexes attractors for grid coding with nested gamma.

INTRODUCTION

Cortical neurons encode information through the rate and timing of their action potential output (Buzsaki and Draguhn, 2004; Fries, 2009; Huxter et al., 2003; O'Keefe and Recce, 1993). At the same time, activity in networks of cortical neurons oscillates with frequency and amplitude that depend on behavioral state (Buzsaki, 2002; Buzsaki and Draguhn, 2004; Buzsaki and Wang, 2012; Canolty and Knight, 2010; Fries, 2009; Klausberger and Somogyi, 2008). Cortical network oscillations are believed to be critical for temporal codes (Buzsaki and Draguhn, 2004; Buzsaki and Wang, 2012; Colgin et al., 2009; Fries, 2009; Lisman, 2005) and coupling between oscillatory activity in different frequency bands appears to be a general feature of cognitive states (Buzsaki and Draguhn, 2004; Buzsaki and Wang, 2012; Canolty and Knight, 2010). However, the cellular mechanisms that coordinate interactions between oscillations in different frequency bands are not known. The relationships between mechanisms that generate oscillatory reference signals and those that support representation of information through firing rate codes are also not clear.

Grid cells in layer II of the medial entorhinal cortex (MEC) represent location relative to the external environment using rate coded grid-like firing fields and by timing of their action potentials relative to theta frequency (4-12 Hz) network rhythms (Fyhn et al., 2004; Hafting et al., 2008; Hafting et al., 2005). Nested within the slower theta rhythm are network oscillations with frequency in the high gamma range (60 - 120 Hz) (Chrobak and Buzsaki, 1998; Colgin et al., 2009). These gamma frequency oscillations are believed to act as a reference signal to coordinate interactions between MEC neurons and their synaptic partners in the hippocampus (Buzsaki and Draguhn, 2004; Colgin et al., 2009), so that ensembles of MEC neurons with firing that is phase-locked to nested gamma oscillations more effectively activate downstream neurons on which their synaptic output converges (Buzsaki and Wang, 2012; Fries, 2009). Nested gamma oscillations are also hypothesized to enable temporal codes in which different items are encoded on each gamma cycle (Lisman, 2005). However, the cellular mechanisms that enable generation of grid firing fields and theta-nested gamma oscillations are not clear. The possibility that theta frequency drive is sufficient for generation of nested gamma oscillations has not previously been addressed. It is also not clear if the same circuit mechanisms generate nested oscillatory activity and grid firing fields, or if instead either form of activity requires additional circuit elements.

Because encoding of location by grid cells in layer II of the MEC requires inputs from the medial septum and as activity of these inputs is modulated at theta frequency (Brandon et al., 2011; Koenig et al., 2011; Mitchell et al., 1982), we set out to investigate whether theta frequency activation of layer II networks is sufficient to generate nested gamma oscillations. Using optogenetic stimulation we demonstrate that theta frequency optical activation elicits nested gamma frequency oscillations that closely resemble activity observed during spatial behaviors. In contrast to pharmacologically induced gamma activity, optical nested oscillations have frequency in the high gamma band and have clock-like properties that make them suitable for multiplexing temporal codes within rate coded firing fields. Optical theta-nested gamma and pharmacologically induced gamma activity also differ in their underlying mechanism. Layer II of the MEC contains inhibitory interneurons and excitatory stellate cells (SCs) that are likely to correspond to grid cells (Burgalossi et al., 2011; Canto et al., 2008; Pastoll et al., 2012a), but the synaptic and functional interactions of SCs and interneurons have not been determined. We establish that nested gamma oscillations require synaptic interactions mediated by local feedback inhibition between SCs, but do not involve recurrent excitation. Finally we demonstrate that networks of excitatory neurons connected only by feedback inhibition are sufficient to generate grid firing fields through network attractor states and to simultaneously produce clock-like theta-nested gamma oscillations.

RESULTS

Local theta frequency stimulation is sufficient to generate nested gamma frequency network oscillations

To test the sufficiency of local theta frequency activity in the MEC for generation of nested gamma frequency oscillations we adopted an optogenetic approach (Figure 1 and Figure S1). We recorded activity from neurons in layer II of the MEC in brain slices prepared from adult mice. We used a mouse line in which expression of channelrhodopsin-2 (ChR2) is under the control of the Thy1 promoter (Arenkiel et al., 2007). In this mouse line all tested SCs and fast-spiking (FS) interneurons were depolarized by light, but pyramidal cells were not (Figure S1). We found that theta frequency (8 Hz) optical stimulation causes local field potential oscillations nested within each theta cycle (Figure 1A-C). This nested activity had frequency 86.1 ± 2.4 Hz (range 62.4 - 100.8 Hz, n = 13), similar to the frequency of nested

gamma activity reported in the MEC of behaving animals (Chrobak and Buzsaki, 1998; Colgin et al., 2009), and much higher than the frequency of pharmacologically induced gamma oscillations (Cunningham et al., 2003; Dickson et al., 2000; Middleton et al., 2008; van Der Linden et al., 1999).

To begin to investigate the synaptic mechanisms mediating nested gamma activity, we recorded membrane currents from SCs. We observed nested synaptic currents with frequency 82.7 ± 2.05 Hz (range 64.2-100.8, n = 21) (Figure 1A-B, D). Cross-correlation analysis indicated that the timing of the nested synaptic currents was similar to simultaneously recorded theta-nested epochs of field gamma activity (peak correlation = 0.81 ± 0.02, lag 0.12 ± 0.2 ms, n = 21)(Figure 1E-F), indicating that they reflect the same process. Consistent with this conclusion, the frequency with maximum power for synaptic and simultaneously recorded field gamma activity was also highly correlated (slope = 0.94, $R^2 = 0.9$, $p = 4.2 \times 10^{-11}$, n = 21).

The nested synaptic currents recorded from SCs were outward going, suggesting that nested gamma oscillations involve inhibitory synaptic input to SCs (Figure 1A). We therefore recorded the membrane potential of SCs and nearby FS interneurons during theta stimulation (Figure 1G). SCs fired on average 1.5 ± 0.2 action potentials per theta epoch (n = 55), whereas interneurons fired 13.4 ± 3.1 spikes per epoch (n = 11)(Figure S1). Theta stimulation modulated the timing of action potential firing by both neuron types (44/48 SCs and 11/11 interneurons $P < 0.05$ vs a uniform distribution, Kuiper test). Within each theta cycle action potential firing by SCs and interneurons coincided with nested gamma oscillations (Figure 1G-I) and the range of theta phases during which interneurons and SCs fired action potentials was similar (mean theta phase of first spike: SC -1.24 rads (from peak), n = 48, FS interneuron -1.72 rads, n = 11, p = 0.79, Non-Parametric Second Order Analysis of angles [NSOA]; mean theta phase of last spike: SC 0.96 rads, n = 37, FS interneuron 1.12 rads, n = 11, p = 0.37 NSOA). However, the distribution of SC and FS interneuron action potential times differed, with SC action potentials following a bimodal distribution with respect to the theta phase, whereas action potentials fired by interneurons followed a broad unimodal distribution ($p = 6 \times 10^{-4}$, NSOA)(Figure 1H-I). The frequency and relative timing of action potentials fired by SCs and interneurons, that we record here during optical theta stimulation, is similar to that recorded from neurons in layer II of the MEC during theta activity in behaving animals (Chrobak and Buzsaki, 1998; Hafting et al., 2008; Mizuseki et al., 2009).

Nested gamma oscillations may enable temporal codes that operate relative to the theta cycle to be superimposed upon firing rate codes (Buzsaki and Wang, 2012; Lisman, 2005). For temporal codes that require predictable reference signals (Fries, 2009; Lisman, 2005), multiplexing of rate and phase codes is likely to be particularly effective if gamma oscillations have clock-like consistency between consecutive theta epochs (Lisman, 2005), but it is not clear how this might be achieved. Surprisingly, we find that while the timing and number of spikes fired by stellate or inhibitory neurons differs between theta cycles, the timing of the gamma oscillations relative to the theta cycle is robust (cf. Figure 1G-I and 2A-B). To quantify the reliability of gamma oscillations we compared the time of each gamma peak during a theta epoch with its average time across all epochs. In many cells each gamma peak fell within a 5 ms window on the majority of theta cycles (Figure 2C). Similarly, even on the fifth gamma peak of each theta cycle, the difference between the time of each gamma peak and the time of the corresponding average peak could be < 3 ms, compared with the gamma period of > 10 ms (Figure 2D). For both measures some, but not all, SCs demonstrate nested gamma activity with timing that is consistent between theta cycles. While the reason for this variability is unclear, these observations nevertheless establish that in principle local theta drive to circuits in the MEC can generate gamma activity with clock-like properties in a substantial fraction of SCs.

To further compare the timing of optically induced nested gamma with activity in vivo, we averaged traces captured by triggering from the negative peak of each gamma oscillation. When nested gamma activity recorded from the MEC of behaving animals is analyzed in this way, average traces contain side peaks adjacent to the central peak, indicating periodicity of the gamma activity (Chrobak and Buzsaki, 1998). Applying this analysis to optically induced nested gamma also reveals side peaks adjacent to the central peak (Figure 2E). This comparison is consistent with the idea that theta-nested gamma oscillations in the entorhinal circuit provide a reference signal for hypothesized coding schemes that require precise temporal coordination of action potential firing (Buzsaki and Wang, 2012; Lisman, 2005).

To test whether the properties of nested gamma oscillations are unique to theta frequency stimulation, we compared responses to optical stimulation at 2, 8 and 16 Hz (Figure S2). With activation at 2, 8 and 16 Hz we observed 23 ± 0.3, 6.6 ± 0.1 and 2.7 ± 0.2 oscillations per stimulus cycle ($p < 10^{-9}$, ANOVA). Although there is no difference in the frequency with

maximum power for 2 Hz compared to 8 Hz stimulation ($p = 0.11$, ANOVA), gamma activity was not as consistently maintained through each 2 Hz cycle, with the result that the total number of gamma cycles available to contribute to information processing is reduced ($p = 0.0003$, t-test). Thus, the phase of maximum gamma power occurred earlier in the stimulation cycle ($p = 0.0005$), the gamma frequency at the trough of the stimulation cycle was lower ($p = 0.005$, $n = 6$) and the gamma activity persevered through a narrower range of the stimulation cycle ($p = 1.1 \times 10^{-6}$). These properties did not differ between 8 Hz and 16 Hz stimulation ($p > 0.1$ for all comparisons). These data suggest that layer II of the MEC is optimized to generate gamma oscillations for approximately half the duration of each theta cycle, but is less effective at sustaining gamma oscillations during stimulation at lower frequencies, while stimulation at higher frequencies generates fewer gamma oscillations per cycle.

Together, these data suggest that theta frequency activation of MEC layer II is sufficient to generate theta-nested gamma activity that resembles activity observed from the MEC of behaving animals (Chrobak and Buzsaki, 1998; Colgin et al., 2009; Lisman, 2005; Mizuseki et al., 2009). In both forms of nested activity the frequency of gamma oscillations is similar, action potential firing by interneurons and excitatory neurons is on the same phase of the theta cycle, and on each theta cycle excitatory neurons fire relatively few spikes, whereas interneurons fire multiple spikes. Nested gamma activity has clock-like properties that may enable it to serve as a reference signal for temporal codes.

Temporally coordinated feedback inhibition mediates nested gamma oscillations

What circuit mechanisms mediate nested gamma oscillations? In principle, gamma frequency oscillatory activity can be generated exclusively by interneuron networks, or by networks that involve coordination of action potential firing by interneurons and excitatory neurons (Buzsaki and Wang, 2012; Fries, 2009; Tiesinga and Sejnowski, 2009). The respective roles of these mechanisms in generating theta-nested gamma oscillations are not clear.

To establish whether synaptic input from excitatory or inhibitory cells is required for nested gamma oscillations we blocked each component of synaptic transmission pharmacologically. Antagonists of ionotropic glutamate receptors (iGluRs) reduced total gamma power by a factor of 5.53 in SCs ($n = 23$, $p = 1.1 \times 10^{-8}$, paired t-test) and a factor of 28.9 in FS interneurons ($n = 5$, $p = 4.4 \times 10^{-4}$, paired t-test). As a result spectral peaks at

gamma frequencies were no longer observed (Figure 3). Antagonists of iGluRs had only very small effects on the mean firing rate (SCs: $p = 0.28$, $n = 24$, FS ints: $p = 0.04$, $n = 8$, paired t-tests) and did not affect theta modulation of firing (Figure S3). The relatively small change in firing rate following block of iGluRs is because the majority of the current driving action potential firing is mediated directly by activation of ChR2 (Figure S3). Therefore the absence of gamma frequency activity during block of iGluRs is not explained by failure of interneurons to generate action potentials during optical theta stimulation. Instead, these data indicate that excitatory synaptic transmission mediated by iGluRs is required to coordinate nested gamma frequency activity.

To determine if theta-nested gamma is generated independently of synaptic connections from neurons in deeper layers of the MEC, and to further investigate differences between optical and pharmacologically induced gamma activity, we recorded from layer II neurons in slices in which the adjacent deeper layers of the MEC have been separated (Figure 3G-H). Blocking NMDA receptors abolishes pharmacologically induced gamma activity generated locally in layer II of the MEC and reveals lower frequency activity that originates from layer III (Middleton et al., 2008). In contrast, we find that optical theta-nested gamma activity is generated in slices in which layers II and III are separated and is maintained after block of NMDA receptors with D-APV (Figure 3G-H). Therefore, optical theta-nested gamma is generated locally in layer II of the MEC and unlike gamma induced pharmacologically in layer II, it does not require activation of NMDA receptors.

We next tested the role of fast inhibitory synaptic transmission. Antagonists of GABA receptors substantially reduced theta-nested gamma activity in SCs (by an average factor of 13.5, $p = 0.02$, $n = 8$, paired t-test) (Figure 4A-C). Block of synaptic inhibition had little effect on the frequency ($p = 0.09$, $n = 7$, paired t-test), or theta modulation of action potentials fired by SCs (Figure S4). Importantly, block of inhibitory synaptic transmission did not reveal excitatory inward currents in recordings from SCs during theta stimulation, even though SCs fired at 13.4 ± 2.7 Hz, suggesting that SCs do not form recurrent excitatory connections with one another. To further test this possibility we drove SCs to fire action potentials using ramp stimuli (Figure 4D-E). Because the ramps switch SCs from silent to active states, we expect them to reveal synaptic responses that depress during prolonged stimulation or that summate from distal locations. Ramp stimuli also did not evoke detectable synaptic responses (Figure 4D-E and Figure S4). Consideration of the numbers of SCs activated in these experiments indicates that the probability of connection

between any two stellate cells is therefore likely to be considerably less than 1 in 500 (Figure S4 and Supplemental Experimental Procedures). These data indicate that nested gamma inputs to SCs originate from GABAergic interneurons and suggest that SCs do not form recurrent excitatory connections with one another.

To further understand the relationship between synaptic responses of SCs and FS interneurons we examined their synaptic connections directly. Action potentials fired by SCs reliably triggered large excitatory synaptic responses in FS interneurons (Fig 4F, H-I), while action potentials fired by FS interneurons triggered inhibitory synaptic responses in SCs (Figure 4G-I). In contrast, action potentials in SCs did not generate synaptic currents in other simultaneously recorded SCs (Figure 4H-I), further supporting our conclusion that direct synaptic connections between SCs are rare or absent. The absence of excitatory synaptic connections between SCs is unlikely to result from our recording conditions, because in the slice preparation that we use axon collaterals from SCs are maintained (Garden et al., 2008), while excitatory synaptic transmission onto SCs and from SCs to other cells is clearly intact (see Figures 3 and 4 and (Garden et al., 2008)). Together with the results of our optogenetic experiments, these data indicate a circuit architecture for nested gamma oscillations, and presumably layer II function in general, whereby SCs interact with one another indirectly via inhibitory interneurons and not through recurrent excitatory connections.

How is the precise timing of the nested gamma oscillations generated? The timing of gamma frequency synaptic currents was strongly correlated between SCs and FS interneurons, with excitatory input to interneurons preceding inhibitory input to SCs by 2.81 ± 0.59 ms (n = 8)(Figure 5A-C). Synaptic currents were synchronized between pairs of nearby SCs with lag < 1 ms, indicating that SCs receive common synchronizing drive from inhibitory neurons (n = 17)(Figure S5). Spikes fired by SCs and interneurons were more likely on the rising phase shortly after the trough of the gamma cycle, but were not precisely locked to a particular gamma phase (Figure 5D-F). The preferred firing phase of SCs was at +0.32 ± 0.02 radians relative to the trough of the synaptic gamma oscillation, whereas firing of interneurons was later at +0.85 ± 0.02 radians ($p = 0.002$, n = 48 SCs, n = 11 interneurons, NSOA). Therefore, excitatory SCs fire near the trough of each gamma cycle just as during exploratory behavior (Chrobak and Buzsaki, 1998). This rapidly triggers spiking by FS interneurons, which then reduce the probability of SC firing until the trough of the next gamma cycle.

Together, these data suggest that coordinated timing of action potentials fired by SCs and FS interneurons mediates theta-nested gamma oscillations. This is distinct from pharmacological models of gamma activity in the MEC in which the frequency of excitatory drive to interneurons is less than the network gamma frequency (Cunningham et al., 2003) and in which NMDA receptor activation is required for oscillations generated within layer II (Middleton et al., 2008). Instead, subsets of SCs firing before the trough of each gamma cycle generate EPSCs in FS interneurons. Action potential firing by FS interneurons then generates feedback inhibition onto SCs. While previous in vivo recordings are consistent with this mechanism (Buzsaki and Wang, 2012), because these experiments were correlative they do not enable synaptic mechanisms to be tested directly. The strength of our approach combining optogenetic and pharmacological manipulation is highlighted by our evidence that, in contrast to previous suggestions based on less direct methods (Beed et al., 2010; Kumar et al., 2007; Quilichini et al., 2010), the primary mechanism for communication between SCs is via inhibitory interneurons.

Feedback inhibition enables generation of grid fields and nested gamma oscillations

To establish if the synaptic connectivity deduced from our experiments can account for nested gamma activity and for generation of grid firing fields, we developed a network model based on our data (Experimental Procedures and Figure S6). Grid firing fields can be generated by networks that produce attractor states (Burak and Fiete, 2009; Fuhs and Touretzky, 2006; Guanella et al., 2007; McNaughton et al., 2006), but except for a model containing exclusively inhibitory interneurons (Burak and Fiete, 2009), previous models rely on direct connections between excitatory cells. This is inconsistent with our finding that SCs communicate primarily via inhibitory interneurons. Previous models also do not generate nested gamma activity. We therefore simulated networks in which excitatory SCs only communicate with one another indirectly via inhibitory neurons, while theta modulated excitatory afferents target both neuron types.

We initially consider a network configuration in which the strongest synapses from inhibitory neurons are onto adjacent excitatory cells, while the strongest connections from excitatory cells are onto a surrounding ring of inhibitory neurons (E-surround configuration)(see Experimental Procedures and Figure S6). This network, which has

connectivity consistent with our experimental data, generates persistent attractor states (Figure 6A). Attractor states in the network are stable during theta stimulation (Figure 6B) and co-exist with theta-nested gamma frequency synaptic oscillations strikingly similar to our experimental data (Figure 6C-H). Comparing gamma activity in consecutive theta epochs, we find that as in the experimental data the gamma signal is clock-like (Figure 6F). The timing of synaptic excitation and inhibition (Fig 6C-E and G-H) is also similar to experimentally induced theta-nested gamma oscillations (cf. Fig 2-5). These simulations demonstrate that feedback inhibition is sufficient to generate network attractor states while also accounting for theta-nested gamma oscillations of activity in the MEC.

We next asked if networks in which excitatory cells communicate only via inhibitory interneurons generate grid firing fields when movement is simulated. Because grid-like firing fields are generated by integration of self-motion signals (Fuhs and Touretzky, 2006; Guanella et al., 2007; McNaughton et al., 2006), we connected synaptic inputs encoding speed of movement in particular directions to subsets of either excitatory or inhibitory neurons (see Experimental Procedures). These inputs move the bump of active neurons according to movement of the animal. Because input from the hippocampus to the MEC is necessary for generation of grid firing fields (Fyhn et al., 2004), a place cell input was also connected to the excitatory cells in the network (Guanella et al., 2007). This input was organized so that place cells project to grid cells that are active at the same location. In the simulations we describe here, this input is active only for 100 ms every 10 s so that spatial firing is determined primarily by integration of the velocity inputs and the place cell input functions to oppose drift in the attractor state.

When velocity inputs are targeted to excitatory neurons the network tracks a wide range of movement velocities and generates grid fields when provided with realistic movement trajectories (Figure 7A-B). When velocity inputs target interneurons, the range of movement velocities that can be tracked is more restricted (Figure 7A), but grid fields are nevertheless indistinguishable from the control network ($p = 0.25$, t-test comparing gridness scores)(Figure 7B). Consistent with experiments in which the hippocampus is lesioned (Fyhn et al., 2004), following removal of the place cell input to the model, grid fields are no longer apparent because of drift in the attractor state ($p = 2.0 \times 10^{-9}$, t-test)(Figures 7C and S7). This drift may result from noise in the network or from the network architecture (Welinder et al., 2008). When the place cell input is activated more frequently, as is likely to be the case in vivo, the network continues to generate grid fields

(not shown). Together, these data establish that theta-modulated attractor networks connected by feedback inhibition are sufficient to generate grid fields. They predict that velocity inputs can effectively target excitatory SCs or inhibitory interneurons and that hippocampal input is required to prevent spontaneous drift in the attractor state.

We next used the model to investigate the relationship between theta activity and grid cell firing. When theta modulated input to the model is replaced by a constant drive of similar mean amplitude, grid fields are maintained ($p = 0.43$ vs control gridness score)(Fig 7D and S7). Models containing exclusively inhibitory interneurons also rely on a constant tonic excitatory drive to generate grid fields and therefore lead to a similar prediction (Burak and Fiete, 2009). This is consistent with the observations that grid fields are present in the absence of theta activity (Yartsev et al., 2011) and that only a subset of grid cells have firing that is modulated at theta frequency (Krupic et al., 2012). It also suggests that abolition of grid fields following septal lesions (Brandon et al., 2011; Koenig et al., 2011) may be due to loss of both an external drive to the network and its theta modulation, in which case the network model also fails to generate grid fields (not shown).

While inhibitory neurons alone are sufficient to represent location (Burak and Fiete, 2009), our experimental data indicate that inhibitory and excitatory neurons must integrate signals they receive from one another. Models that incorporate only one neuron type do not specify how this is done, whether firing fields of interneurons and excitatory neurons differ or if variations in connectivity lead to different predictions for spatial firing or nested gamma activity. We therefore investigated the firing properties of inhibitory neurons and the consequences of different organizations of connections between excitatory and inhibitory neurons. We find that inhibitory neurons in the E-surround network configuration encode location (Figure 7F). However, unlike in models containing only inhibitory neurons (Burak and Fiete, 2009), interneurons in the E-surround network have inverted grid fields (Figure 7F). We next investigated networks in which the strongest inhibition is onto a ring of excitatory SCs, but the strongest excitation is local (I-surround configuration)(Figure 7E). Excitatory neurons in this configuration also have grid fields and theta-nested gamma oscillations in their synaptic input (Figure 7G and S7). In this configuration, interneurons have grid fields that are similar to those of excitatory cells (grid score 1.07 ± 0.01 and 1.08 ± 0.01 for excitatory and inhibitory cells respectively, $p = 0.78$, t-test). Multiple peaks in the 2D Fourier transform of grid fields recorded in behaving animals could indicate that spatial firing originates from upstream band cells rather than from an attractor network of the kind

we characterize here (Krupic et al., 2012). However, in both model configurations 2D Fourier spectrograms of the firing field have multiple peaks even though band cells are not found in either configuration, indicating that these peaks do not necessarily imply the existence of upstream band cells (Figure 7B, D, F-G). We nevertheless found that leaving intact only one direction of velocity input to either network leads to emergence of band cells (Figure S7). In this case both networks continue to generate theta-nested gamma oscillations. Together these data indicate that theta-nested gamma oscillatory activity is a general feature of attractor networks that generate representations of space using indirect inhibitory interactions between excitatory cells. They also demonstrate that the nature of spatial representation by interneurons depends on the organization of connections within the network.

Our simulations lead to a number of new predictions about the membrane potential dynamics of SCs during behavior (Figure 8). Theta-nested gamma frequency synaptic activity is found in both neuron types in E- and I-surround configurations of the model (Figure 8B-C, G-H, L-M). In both model configurations excitatory neurons fire action potentials soon after the trough of gamma (Figure 8D), while firing by interneurons is typically later in the gamma cycle (Figure 8I, N). Inhibition to SCs and excitation to interneurons varies as a function of distance from the center of the firing field ($R^2 = 0.61$, $p < 10^{-9}$ and $R^2 = 0.63$, $p < 10^{-9}$ respectively for the E-surround model and $R^2 = 0.66$, $p < 10^{-9}$ and $R^2 = 0.63$, $p < 10^{-9}$ for the I surround model)(Figure 8E, J, O). In all configurations the synaptic drive to excitatory and inhibitory neurons coincides with the depolarizing component of the theta input and the amplitude of the gamma frequency inhibitory input to SCs is greatest outside the firing field and weakest at the center of the firing field. However, in the E-surround configuration, gamma frequency excitation of interneurons is strongest on the edges of the inverted firing field and weakest at the center (Figure 8G-H, J). In contrast, in the I-surround configuration this relationship is reversed (Figure 8L-M, O). Together, these data predict that in individual grid cells the amplitude of theta-nested gamma depends on an animal's location.

DISCUSSION

We demonstrate that theta frequency activation of layer II of the MEC generates nested gamma frequency oscillations that resemble activity observed during spatial behaviors. We find that feedback inhibition is the primary mode of communication between SCs and is

sufficient to account for nested gamma oscillations. While the activity of individual neurons varies between gamma cycles, coordination of synaptic inhibition and excitation nevertheless results in gamma oscillations with clock-like timing suitable for use as a reference signal in temporal codes. We show that feedback inhibition is also sufficient for emergence of attractor states that co-exist with nested gamma oscillations and that generate rate-coded grid firing fields. Therefore grid firing fields and theta-nested gamma oscillations may result from a common local circuit architecture, which is defined by communication between SCs mediated primarily via inhibitory interneurons.

The optically induced nested gamma activity that we describe here has key features in common with theta-nested gamma oscillations observed during spatial exploration. These include a similar frequency (60 - 100 Hz) (Chrobak and Buzsaki, 1998; Colgin et al., 2009), activation of FS interneurons and excitatory cells at similar phases of the theta oscillation (Chrobak and Buzsaki, 1998; Mizuseki et al., 2009), and similar timing of action potentials relative to the nested gamma oscillation (Chrobak and Buzsaki, 1998). Both forms of theta-nested gamma activity appear to be mechanistically distinct from pharmacologically induced gamma oscillations, which have much lower frequency (30 - 45 Hz), no clear relationship to theta activity and different involvement of NMDA receptors (Cunningham et al., 2003; Dickson et al., 2000; Middleton et al., 2008; van Der Linden et al., 1999). Signatures of clock-like activity found during optical theta-nested gamma (Figure 2) are also apparent during in vivo theta-nested gamma activity (Chrobak and Buzsaki, 1998), indicating that circuits in layer II of the MEC contain cellular machinery to generate reference signals for temporal coding (Buzsaki and Draguhn, 2004; Lisman, 2005).

Understanding brain computations requires knowledge of the wiring of neuronal circuits. In many cortical areas, including deeper layers of the MEC (Dhillon and Jones, 2000), information is transmitted directly between nearby excitatory neurons (Deuchars et al., 1994; Mason et al., 1991; Song et al., 2005). Axons of SCs have collaterals in layer II of the MEC (Burgalossi et al., 2011; Garden et al., 2008; Quilichini et al., 2010), which have been suggested to form recurrent excitatory connections (Beed et al., 2010; Kumar et al., 2007). However, we did not observe excitatory synaptic responses when large populations of SCs fire action potentials (Figure 4A and S4) indicating that SCs in layer II of the MEC do not communicate directly with one another. This is consistent with recordings from pairs of SCs (Figure 4F-I and (Dhillon and Jones, 2000)). By demonstrating connections in both

directions between SCs and interneurons, our data instead indicate that communication between SCs in layer II of the MEC is primarily through feedback inhibition.

Because SCs in layer II of the MEC are likely to be grid cells (Burgalossi et al., 2011; Canto et al., 2008; Pastoll et al., 2012a), elucidation of their local connectivity and their role in oscillatory network activity is critical to understanding grid firing fields. Our finding that SCs communicate primarily by feedback inhibition argues against models that rely on direct excitation between grid cells (Fuhs and Touretzky, 2006; Guanella et al., 2007; Navratilova et al., 2011). Instead, it supports the theoretical prediction that inhibition can mediate grid firing fields (Burak and Fiete, 2009), but suggests this is implemented using interactions between inhibitory interneurons and SCs rather than through direct inhibitory connections between grid cells. Nevertheless, while our model establishes the sufficiency of inhibitory feedback for generation of attractor states by SCs, the actual network may depend on interactions between layers for its functionality, while other details of the model that enable it to generate spatial representations are not yet well constrained. For example, in our model velocity and theta inputs target grid cells directly, but they could also arrive indirectly via neurons in deeper layers of the MEC (Navratilova et al., 2012).

By exploring models in which SCs communicate solely by feedback inhibition, we make several new predictions. First, interneurons may have spatial firing fields. An E-surround network configuration causes interneurons to have inverted grid firing fields, whereas an I-surround configuration causes interneurons to have fields with grid scores similar to excitatory neurons (Figure 7). Consistent with these predictions, interneurons with spatial firing fields defined by a decrease in firing frequency have been identified in the hippocampus (McNaughton et al., 1983; Wilent and Nitz, 2007), although to our knowledge spatial firing has not been investigated for entorhinal interneurons. Second, the role of theta frequency input can be dissociated into a tonic drive, which is required for grid cell firing, and phasic theta modulation of that drive, which is required for generation of clock-like nested gamma oscillations (Figure 7E). This is consistent with previous data (Brandon et al., 2011; Koenig et al., 2011; Yartsev et al., 2011), but remains to be tested directly. Third, recording of the membrane potential of SCs in behaving animals should reveal gamma frequency IPSPs on the depolarizing phase of theta with amplitude that decreases with distance from the center of the firing field (Figure 8). In contrast, recording from FS interneurons should reveal gamma frequency EPSPs on the depolarizing phase of theta with amplitude relative to the firing field that depends on whether the network has

an E-surround or an I-surround configuration (Figure 8). While our model is no doubt considerably simplified compared to the layer II network in behaving animals, experimental corroboration of these predictions would lend strong support to the architecture that we outline here as a basis for generation of grid firing fields.

What is the function of theta-nested gamma oscillations? Our results suggest a cellular substrate for several theories of temporal coding. First, nested gamma oscillations may enable coincident firing of ensembles of SCs within time windows required for coincidence detection by downstream neurons in the dentate gyrus (Buzsaki and Wang, 2012; Chrobak and Buzsaki, 1998). Second, phase locking of nested gamma oscillations between different regions may control the efficacy of their interactions with up- or downstream networks (Buzsaki and Wang, 2012; Fries, 2009). In this scenario, temporal codes require that interacting brain areas generate theta-nested gamma activity of a similar frequency, with the gain of the interaction depending on the relative phases of the gamma activity. Third, nested gamma oscillations may be used in more complex schemes for temporal encoding of sequences in which distinct information is encoded within each gamma cycle (Lisman, 2005). This may include theta phase precession of action potentials for which the role of gamma activity is not yet clear (Lisman, 2005). While generation of gamma oscillations alone is sufficient for the first coding scheme, the other schemes rely on precise temporal relationships between theta and gamma (Buzsaki and Wang, 2012). Different properties of gamma activated by different frequencies of optical stimulation may reflect optimization of the circuit for these coding schemes (Figure S2).

In conclusion, our data provide evidence that feedback inhibition accounts for two well established features of network activity in behaving animals. Our experiments and model recapitulate defining features of theta-nested gamma activity that is observed from neurons in the MEC and other brain areas (Chrobak and Buzsaki, 1998; Colgin et al., 2009; Lisman, 2005; Mizuseki et al., 2009). We establish that the circuit elements that produce gamma oscillations phase locked to theta can do so with remarkable trial-to-trial consistency, suggesting that the local MEC circuit has clock-like properties required for reference signals for neuronal computations that rely on the timing of gamma oscillations (Buzsaki and Wang, 2012; Fries, 2009; Lisman, 2005). The simple principles for organization of the MEC circuit derived from these experiments also account for generation of grid-like firing fields. These results suggest that common circuit mechanisms evolved to support simultaneous rate and temporal coding in the central nervous system.

EXPERIMENTAL PROCEDURES

Electrophysiological recordings

All experiments used adult (7 - 9 week old) mice from Thy1-ChR2-YFP line 18 (Arenkiel et al., 2007). Sagittal brain slices were prepared and whole-cell patch-clamp recordings made as described previously (Garden et al., 2008; Pastoll et al., 2012b). The slices include all layers and the full dorsal-ventral extent of the MEC. Illumination for activation of ChR2 was from a 470 nM colllimated LED (Thorlabs) introduced through the epifluorescence port of the microscope (Olympus BX-51) and focused onto the slice from above (Figure S1). The region of neurons activated by light had a radius of approximately 100 μm. Pharmacological agents were bath applied to the whole slice.

Attractor network model

A network of exponential integrate and fire neurons (Fourcaud-Trocme et al., 2003) was implemented using the Brian simulator (Goodman and Brette, 2008). Full details of parameter values and explanation of the model are in the Supplemental Experimental Procedures.

In the model each neuron received an external current source composed of the sum of constant background activation, theta modulated current simulated as cosine function, velocity modulation current and hippocampal place field input. To simulate noise, independent Gaussian distributed current was injected to give a 2 mV standard deviation in the resting membrane potential of each neuron.

Network topology and Connectivity. The network consisted of 68 x 58 excitatory cells and 34 x 30 interneurons uniformly distributed on a twisted torus (Guanella et al., 2007). In the E-surround configuration connections from excitatory to inhibitory cells used AMPA and NMDA type conductances and their topography followed a ring-like organization with an appropriate offset for implementation of velocity modulation, while the topography of inhibitory to excitatory connections had a Gaussian profile (Figure S6A-B, Figure 7E). In the I-surround configuration, the topography of the excitatory to inhibitory connections followed the Gaussian profile, while the connections from inhibitory to excitatory neurons followed the ring-like organization.

Velocity modulation. To perform path integration the activity in the network must propagate along the direction of the simulated movement of the animal (Fuhs and Touretzky, 2006; Guanella et al., 2007; McNaughton et al., 2006). This is achieved by shifting the center of the synaptic profile of neurons in one of the populations (excitatory or inhibitory), in the direction of preferred movement. Each neuron was assigned a directional vector from a group of four directions (up, down, left, right) and its outgoing synaptic weight profile was shifted by a predefined constant. During simulated movement a velocity-modulated current was then injected into the neuron (Figure S6C). To evaluate spatial representation by the network during exploration, 15-20 minutes of movement was simulated. At each time point the velocity vector was estimated as a forward difference of published positional data (Hafting et al., 2005).

Place cell input. Because action potential firing and noise lead to slow drift in the state of the network, unless otherwise stated simulations contain an allothetic input from place cells that is active for 100 ms every 10 s and opposes the drift.

Data analysis and statistics

Electrophysiology and simulation data were analyzed using built in and custom routines in IGORpro, Matlab or Python. Comparisons between groups used ANOVA and Student's t-test as indicated. For simulations, networks receiving a theta input and velocity modulation of the excitatory cells are considered as the control group. Gridness scores are calculated following previous studies (Sargolini et al., 2006). Full details for analysis of oscillatory and grid activity are given in the Supplemental Experimental Procedures.

References

Arenkiel, B.R., Peca, J., Davison, I.G., Feliciano, C., Deisseroth, K., Augustine, G.J., Ehlers, M.D., and Feng, G. (2007). In vivo light-induced activation of neural circuitry in transgenic mice expressing channelrhodopsin-2. Neuron *54*, 205-218.

Beed, P., Bendels, M.H., Wiegand, H.F., Leibold, C., Johenning, F.W., and Schmitz, D. (2010). Analysis of excitatory microcircuitry in the medial entorhinal cortex reveals cell-type-specific differences. Neuron *68*, 1059-1066.

Brandon, M.P., Bogaard, A.R., Libby, C.P., Connerney, M.A., Gupta, K., and Hasselmo, M.E. (2011). Reduction of theta rhythm dissociates grid cell spatial periodicity from directional tuning. Science *332*, 595-599.

Burak, Y., and Fiete, I.R. (2009). Accurate path integration in continuous attractor network models of grid cells. PLoS Comput Biol *5*, e1000291.

Burgalossi, A., Herfst, L., von Heimendahl, M., Forste, H., Haskic, K., Schmidt, M., and Brecht, M. (2011). Microcircuits of functionally identified neurons in the rat medial entorhinal cortex. Neuron *70*, 773-786.

Buzsaki, G. (2002). Theta oscillations in the hippocampus. Neuron *33*, 325-340.

Buzsaki, G., and Draguhn, A. (2004). Neuronal oscillations in cortical networks. Science *304*, 1926-1929.

Buzsaki, G., and Wang, X.J. (2012). Mechanisms of Gamma Oscillations. Annu Rev Neurosci.

Canolty, R.T., and Knight, R.T. (2010). The functional role of cross-frequency coupling. Trends Cogn Sci *14*, 506-515.

Canto, C.B., Wouterlood, F.G., and Witter, M.P. (2008). What does the anatomical organization of the entorhinal cortex tell us? Neural Plast *2008*, 381243.

Chrobak, J.J., and Buzsaki, G. (1998). Gamma oscillations in the entorhinal cortex of the freely behaving rat. J Neurosci *18*, 388-398.

Colgin, L.L., Denninger, T., Fyhn, M., Hafting, T., Bonnevie, T., Jensen, O., Moser, M.B., and Moser, E.I. (2009). Frequency of gamma oscillations routes flow of information in the hippocampus. Nature *462*, 353-357.

Cunningham, M.O., Davies, C.H., Buhl, E.H., Kopell, N., and Whittington, M.A. (2003). Gamma oscillations induced by kainate receptor activation in the entorhinal cortex in vitro. J Neurosci *23*, 9761-9769.

Deuchars, J., West, D.C., and Thomson, A.M. (1994). Relationships between morphology and physiology of pyramid-pyramid single axon connections in rat neocortex in vitro. J Physiol *478 Pt 3*, 423-435.

Dhillon, A., and Jones, R.S. (2000). Laminar differences in recurrent excitatory transmission in the rat entorhinal cortex in vitro. Neuroscience *99*, 413-422.

Dickson, C.T., Biella, G., and de Curtis, M. (2000). Evidence for spatial modules mediated by temporal synchronization of carbachol-induced gamma rhythm in medial entorhinal cortex. J Neurosci *20*, 7846-7854.

Fourcaud-Trocme, N., Hansel, D., van Vreeswijk, C., and Brunel, N. (2003). How spike generation mechanisms determine the neuronal response to fluctuating inputs. J Neurosci *23*, 11628-11640.
Fries, P. (2009). Neuronal gamma-band synchronization as a fundamental process in cortical computation. Annu Rev Neurosci *32*, 209-224.
Fuhs, M.C., and Touretzky, D.S. (2006). A spin glass model of path integration in rat medial entorhinal cortex. J Neurosci *26*, 4266-4276.
Fyhn, M., Molden, S., Witter, M.P., Moser, E.I., and Moser, M.B. (2004). Spatial representation in the entorhinal cortex. Science *305*, 1258-1264.
Garden, D.L., Dodson, P.D., O'Donnell, C., White, M.D., and Nolan, M.F. (2008). Tuning of synaptic integration in the medial entorhinal cortex to the organization of grid cell firing fields. Neuron *60*, 875-889.
Goodman, D., and Brette, R. (2008). Brian: a simulator for spiking neural networks in python. Front Neuroinform *2*, 5.
Guanella, A., Kiper, D., and Verschure, P. (2007). A model of grid cells based on a twisted torus topology. Int J Neural Syst *17*, 231-240.
Hafting, T., Fyhn, M., Bonnevie, T., Moser, M.B., and Moser, E.I. (2008). Hippocampus-independent phase precession in entorhinal grid cells. Nature *453*, 1248-1252.
Hafting, T., Fyhn, M., Molden, S., Moser, M.B., and Moser, E.I. (2005). Microstructure of a spatial map in the entorhinal cortex. Nature *436*, 801-806.
Huxter, J., Burgess, N., and O'Keefe, J. (2003). Independent rate and temporal coding in hippocampal pyramidal cells. Nature *425*, 828-832.
Klausberger, T., and Somogyi, P. (2008). Neuronal diversity and temporal dynamics: the unity of hippocampal circuit operations. Science *321*, 53-57.
Koenig, J., Linder, A.N., Leutgeb, J.K., and Leutgeb, S. (2011). The spatial periodicity of grid cells is not sustained during reduced theta oscillations. Science *332*, 592-595.
Krupic, J., Burgess, N., and O'Keefe, J. (2012). Neural representations of location composed of spatially periodic bands. Science *337*, 853-857.
Kumar, S.S., Jin, X., Buckmaster, P.S., and Huguenard, J.R. (2007). Recurrent circuits in layer II of medial entorhinal cortex in a model of temporal lobe epilepsy. J Neurosci *27*, 1239-1246.
Lisman, J. (2005). The theta/gamma discrete phase code occuring during the hippocampal phase precession may be a more general brain coding scheme. Hippocampus *15*, 913-922.

Mason, A., Nicoll, A., and Stratford, K. (1991). Synaptic transmission between individual pyramidal neurons of the rat visual cortex in vitro. J Neurosci *11*, 72-84.
McNaughton, B.L., Barnes, C.A., and O'Keefe, J. (1983). The contributions of position, direction, and velocity to single unit activity in the hippocampus of freely-moving rats. Exp Brain Res *52*, 41-49.
McNaughton, B.L., Battaglia, F.P., Jensen, O., Moser, E.I., and Moser, M.B. (2006). Path integration and the neural basis of the 'cognitive map'. Nat Rev Neurosci *7*, 663-678.
Middleton, S., Jalics, J., Kispersky, T., Lebeau, F.E., Roopun, A.K., Kopell, N.J., Whittington, M.A., and Cunningham, M.O. (2008). NMDA receptor-dependent switching between different gamma rhythm-generating microcircuits in entorhinal cortex. Proc Natl Acad Sci U S A *105*, 18572-18577.
Mitchell, S.J., Rawlins, J.N., Steward, O., and Olton, D.S. (1982). Medial septal area lesions disrupt theta rhythm and cholinergic staining in medial entorhinal cortex and produce impaired radial arm maze behavior in rats. J Neurosci *2*, 292-302.
Mizuseki, K., Sirota, A., Pastalkova, E., and Buzsaki, G. (2009). Theta oscillations provide temporal windows for local circuit computation in the entorhinal-hippocampal loop. Neuron *64*, 267-280.
Navratilova, Z., Giocomo, L.M., Fellous, J.M., Hasselmo, M.E., and McNaughton, B.L. (2011). Phase precession and variable spatial scaling in a periodic attractor map model of medial entorhinal grid cells with realistic after-spike dynamics. Hippocampus.
Navratilova, Z., Giocomo, L.M., Fellous, J.M., Hasselmo, M.E., and McNaughton, B.L. (2012). Phase precession and variable spatial scaling in a periodic attractor map model of medial entorhinal grid cells with realistic after-spike dynamics. Hippocampus *22*, 772-789.
O'Keefe, J., and Recce, M.L. (1993). Phase relationship between hippocampal place units and the EEG theta rhythm. Hippocampus *3*, 317-330.
Pastoll, H., Ramsden, H.L., and Nolan, M.F. (2012a). Intrinsic electrophysiological properties of entorhinal cortex stellate cells and their contribution to grid cell firing fields. Front Neural Circuits *6*, 17.
Pastoll, H., White, M., and Nolan, M. (2012b). Preparation of Parasagittal Slices for the Investigation of Dorsal-ventral Organization of the Rodent Medial Entorhinal Cortex. J Vis Exp.
Quilichini, P., Sirota, A., and Buzsaki, G. (2010). Intrinsic circuit organization and theta-gamma oscillation dynamics in the entorhinal cortex of the rat. J Neurosci *30*, 11128-11142.

Sargolini, F., Fyhn, M., Hafting, T., McNaughton, B.L., Witter, M.P., Moser, M.B., and Moser, E.I. (2006). Conjunctive representation of position, direction, and velocity in entorhinal cortex. Science *312*, 758-762.
Song, S., Sjostrom, P.J., Reigl, M., Nelson, S., and Chklovskii, D.B. (2005). Highly nonrandom features of synaptic connectivity in local cortical circuits. PLoS Biol *3*, e68.
Tiesinga, P., and Sejnowski, T.J. (2009). Cortical enlightenment: are attentional gamma oscillations driven by ING or PING? Neuron *63*, 727-732.
van Der Linden, S., Panzica, F., and de Curtis, M. (1999). Carbachol induces fast oscillations in the medial but not in the lateral entorhinal cortex of the isolated guinea pig brain. J Neurophysiol *82*, 2441-2450.
Welinder, P.E., Burak, Y., and Fiete, I.R. (2008). Grid cells: the position code, neural network models of activity, and the problem of learning. Hippocampus *18*, 1283-1300.
Wilent, W.B., and Nitz, D.A. (2007). Discrete place fields of hippocampal formation interneurons. J Neurophysiol *97*, 4152-4161.
Yartsev, M.M., Witter, M.P., and Ulanovsky, N. (2011). Grid cells without theta oscillations in the entorhinal cortex of bats. Nature *479*, 103-107.

Acknowledgements

This work was supported by the Biotechnology and Biological Sciences Research Council (M.F.N.), the Engineering and Physical Sciences Research Council (H.P. and L.S.) and the Commonwealth Scholarships Commission (H.P.). We thank Ian Duguid for comments on the manuscript and Patrick Kaifosh for suggestions about network configurations. This work made use of resources provided by the Edinburgh Compute and Data Facility.

Author-contributions

HP contributed to design of the study, performed and analyzed experiments. LS contributed to design of the study, performed and analyzed simulations. MCWvR contributed to design of the study and analysis of simulations. MFN designed and supervised the study, contributed to data analysis and wrote the manuscript.

Figure 1. Theta frequency stimulation drives nested gamma oscillations

(A) Example of extracellular field activity and membrane current recorded from a SC during theta modulated (8 Hz) optical stimulation of layer II of the MEC, illustrating gamma oscillations nested within each theta cycle. The field recording is also shown band pass filtered to separate theta and gamma activity.
(B) Scalograms of field (upper) and synaptic (lower) activity corresponding to data in (A), plotting power for each frequency as a function of time. In all figures the power corresponding to the maximum of the color scale is indicated in the lower right of each plot.
(C, D) Mean scalograms from all recordings of field (C)(n = 27) and SC synaptic activity (D)(n = 44) as a function of phase of theta stimulation.
(E) Cross-correlations between field potential and SC membrane currents (peak correlation = 0.81 ± 0.02, lag 0.12 ± 0.2 ms, n = 21). Example from (A-B) is in black, all other experiments are in grey.
(F) Histogram of lag between field and SC synaptic activity calculated from (E).
(G) Examples of action potentials fired by a SC and a FS interneuron recorded simultaneously during 8 Hz light stimulation, illustrating that both neuron types fire action potentials on the phase of the theta cycle at which nested gamma oscillations are observed.
(H) Rasters of spikes fired by neurons in (G) for 40 consecutive theta epochs.
(I) Probability of SC and FS interneuron action potentials with respect to the phase of theta stimulation. Solid lines are the population means, dashed lines are the examples from (G).

Figure 2. Clock-like properties of nested gamma activity
(A) Example of a membrane current recorded from a SC during a theta cycle (upper) and corresponding filtered current (lower, colored line). Also shown are filtered traces from 4 adjacent theta epochs (grey traces), illustrating the consistency of the nested gamma response between theta cycles.
(B) Heat map of membrane currents during 40 consecutive cycles of theta stimulation from the cell in (A). Color scale corresponds to (A).
(C-D) Fraction of gamma cycles on which the peak current differs by less than ± 5 ms (C) and average offset of individual gamma cycles compared to the mean (D) are plotted as a function of the index of each nested gamma peak. Open circles correspond to individual neurons and filled bars indicate the mean ± SEM (n = 12).

(E) Examples of traces obtained by averaging responses triggered from the trough of each gamma cycle recorded simultaneously from a SC (upper) and the nearby field (lower). The side peaks are consistent with periodic gamma activity.

Figure 3. Nested gamma oscillations require feedback inhibition

(A) Example of nested gamma frequency synaptic currents recorded from a SC before (control) and during block of iGluRs (NBQX + D-APV).

(B) Scalograms for all theta epochs from experiment in (a) in control (upper) and after block of iGluRs with NBQX and D-APV (lower), demonstrating that iGluRs are required for nested gamma activity.

(C) Mean data from all experiments indicating total power in control conditions and during block of iGluRs (n = 23, $p = 1.1 \times 10^{-8}$, paired t-test). Data are log transformed to reduce the variance for statistical testing.

(D-F) As for (A-C) except that data are for FS interneurons. For (F), n = 5 and $p = 4.4 \times 10^{-4}$.

(G) Schematic indicates the slice cut to separate layers II and III (left). Examples of synaptic currents (row 2), corresponding scalograms (row 3) and the mean scalograms for all experiments (row 4), each plotted as a function of the phase of theta stimulation, demonstrate that nested gamma is maintained when connections between layer II and III are cut (control) and after subsequent block of NMDA receptors with 50 μM D-APV, but is abolished by complete block of iGluRs.

(H) Mean power is not significantly different following block of NMDA receptors (p = 0.53, n = 6, paired t-test), but is then reduced by complete block of iGluRs (p = 0.0015).

Figure 4. Feedback inhibition without recurrent excitation mediates interactions between stellate cells

(A) Examples of membrane currents recorded from a SC during theta frequency network stimulation (upper) in control conditions (middle) and during block of GABA receptors with picrotoxin (50 μM) and CGP55845 (1 μM) (lower). Outward going synaptic currents are abolished when GABA receptors are blocked. Even after block of inhibition inward synaptic currents are not observed indicating that SCs do not form excitatory connections to one another.

(B) Average scalogram of synaptic activity recorded from the SC in (A) before (upper) and during block of GABA receptors (lower).

(C) Total power of the largest peak in the scalogram is reduced by block of GABA receptors (n = 7, p = 0.02).
(D-E) Example of membrane potential (D) and current (E) of a SC during ramp-like optical activation of layer II in control conditions (upper trace) and subsequently during block of GABA receptors (lower). Although the optical stimulus drives action potential firing at high frequencies (D), excitatory synaptic currents are not observed (E), further indicating that SCs do not form direct synaptic connections with one another. Traces in the boxed regions in (E) are shown below on an expanded time scale.
(F) Example of synaptic response of a FS interneuron to an action potential in a simultaneously recorded presynaptic SC.
(G) Example of synaptic response of a SC to an action potential in a simultaneously recorded presynaptic FS interneuron.
(H-I) Number of pairs (H) and probability of functional connections for the pairs tested (I), for pairs of SCs (S-S), presynaptic SC to postsynaptic FS interneuron (SC -> interneuron) and presynaptic FS interneuron to postsynaptic SCs (interneuron -> SC).

Figure 5. Temporal organization of synaptic events and action potential activity during nested gamma oscillations

(A) Example of synaptic currents recorded simultaneously from a FS interneuron and a SC during a single cycle of theta frequency stimulation.
(B) Detail of regions in (A) indicated by the box, demonstrates that excitatory input to interneurons arrives before inhibitory input to SCs.
(C) Cross-correlation between SC and FS interneuron membrane currents during theta stimulation for the example in (A-B) and for 7 other experiments indicates that excitation to interneurons consistently leads inhibition to SCs (maximum correlation = 0.56 ± 0.07, lag = 2.81 ± 0.59 ms, n = 8).
(D) Example of simultaneously recorded FS interneuron, SC and extracellular field potential during a single epoch of theta stimulation.
(E) Detail from (D) illustrating action potential initiation in the stellate cell earlier in the gamma cycle and preceding action potential initiation in the FS interneuron.
(F) The probability of action potential initiation as a function of phase of the local field potential gamma signal for interneurons (upper) and SCs (lower) for the example recordings in (D-E)(left) and on average for all recordings (right).

Figure 6. Clock-like nested gamma oscillations are generated by attractor networks of neurons connected only through recurrent inhibition

(A) A snapshot of neuronal activity as a function of position in the 68 x 58 layer of excitatory neurons. Data in this figure are from the network in the E-surround configuration, but similar results are obtained using the I-surround configuration.

(B) Spike rasters from 68 neurons corresponding to row 29 in (A), indicating stability of the bump during successive theta cycles.

(C) Examples of synaptic currents recorded from inhibitory and excitatory neurons at the center of the activity bump in (A).

(D-E) Synaptic currents during a single gamma cycle (D), and the cross-correlation between synaptic currents recorded from excitatory and inhibitory neurons (E), illustrate how excitatory input to interneurons precedes inhibitory input to excitatory neurons. Both examples are from the neuron pair in (C).

(F) Synaptic currents from 40 consecutive theta cycles plotted on a color scale indicate the consistent timing of nested gamma oscillations across theta cycles. Data are from an excitatory neuron at the center of the activity bump in the model network described in (A-E). Similar clock-like nested gamma responses are observed from neurons at all locations.

(G) Action potential rasters for a cell at the center of the bump as in (F) for 40 consecutive theta epochs. The timing, but not the number of action potentials, is similar on each theta cycle.

(H) Example scalogram of membrane current power during 40 consecutive theta cycles for the neuron in (F-G).

Figure 7. Theta-Nested gamma oscillations co-exist with, but are not necessary for, grid firing fields

(A) Speed of movement of the attractor bump is plotted as a function of the amplitude of the input encoding movement velocity for networks with differing offset in the outgoing connection profile from excitatory to inhibitory cells. Networks in which movement velocity drives excitatory neuron firing (upper) maintain a wider linear response range than networks in which movement inputs are targeted to interneurons.

(B) Examples heat maps for firing (upper), corresponding autocorrelation plots (middle) and 2D Fourier spectrograms (lower) generated by simulated exploration of the arena using attractor models with velocity input to excitatory cells (left) or inhibitory cells (right). Gridness scores do not differ between networks with velocity input to excitatory neurons (E cells) (1.1 ± 0.01, $n = 10$) and inhibitory neurons (I cells) (1.12 ± 0.01, $n = 10$, $p = 0.25$).

(C) Simulation in the absence of place input. The firing fields have a gridness score of 0.22 ± 0.07, which is substantially less than that of control neurons ($p = 1.16 \times 10^{-9}$ n = 15), indicating that grid firing is absent.
(D) Simulations in which theta frequency modulation of network drive is removed. Grid fields have a gridness score of 1.11 ± 0.01 and are similar to control grid fields (n = 10, P=0.43). Scales bar for firing fields in B-D is 60 cm.
(E) Synaptic conductance is plotted as a function of distance between neurons normalized to the size of the neurons sheet for connections from E cells to I cells (Excitation) and from I cells to E cells (Inhibition) for E-surround (upper) and I-surround (lower) versions of the model.
(F) Predicted interneuron firing fields for the E-surround model configuration. The field appears as an inverted grid field such that the grid apex has a low firing rate and the region between the apices is coded by a high firing rate.
(G) Firing rate maps (upper), spatial autocorrelations (middle) and 2D Fourier spectrograms (lower) for example excitatory (left) and inhibitory (middle) neurons in the I-surround configuration. This network configuration also generates theta-nested gamma activity illustrated by synaptic currents during a single theta cycle and the scalogram of the inhibitory currents as a function of theta cycle phase (right).
Scale bars are 60 cm for the rate and autocorrelation plots and 4 m^{-1} for the Fourier spectrograms.

Figure 8. Predicted membrane potential and current dynamics associated with grid firing fields

(A) Location of the exemplar neurons in the excitatory cell layer with respect to the activity bump. Each color-coded point represents the firing frequency of a single neuron. Network is in the E-surround configuration, but results for excitatory cells are similar in the I-surround configuration.
(B-C) Membrane potential and current during two theta cycles for neurons at the locations indicated in (A). Both neurons received nested gamma frequency inhibitory input, but this is lower at the center of the bump, enabling the external theta drive to trigger action potential firing.
(D) Spike probability as a function of gamma phase for the excitatory neurons.

(E) Total charge during each theta cycle of the inhibitory synaptic input to an excitatory cell plotted as a function of distance from the center of the excitatory cell's nearest grid firing field during that cycle.
(F) Location of the exemplar neurons in the inhibitory cell layer in the E-surround network configuration. The activity bump is inverted with respect to the excitatory cell layer.
(G-H) Membrane potential and current during two theta cycles for neurons at the locations indicated in (F). Both neurons received nested gamma frequency excitatory input, but this is lower for interneurons that project onto excitatory cells at the center of the bump.
(I) Spike probability as a function of gamma phase for the inhibitory neurons.
(J) Total charge during each theta cycle of the excitatory synaptic input to an inhibitory cell plotted as a function of distance during that cycle from the center of the nearest grid firing field of the excitatory cell to which the inhibitory neuron makes strongest connections.
(K-O) As for (F-J) except for a network in the I-surround configuration.

Figure 1

Click here to download high resolution image

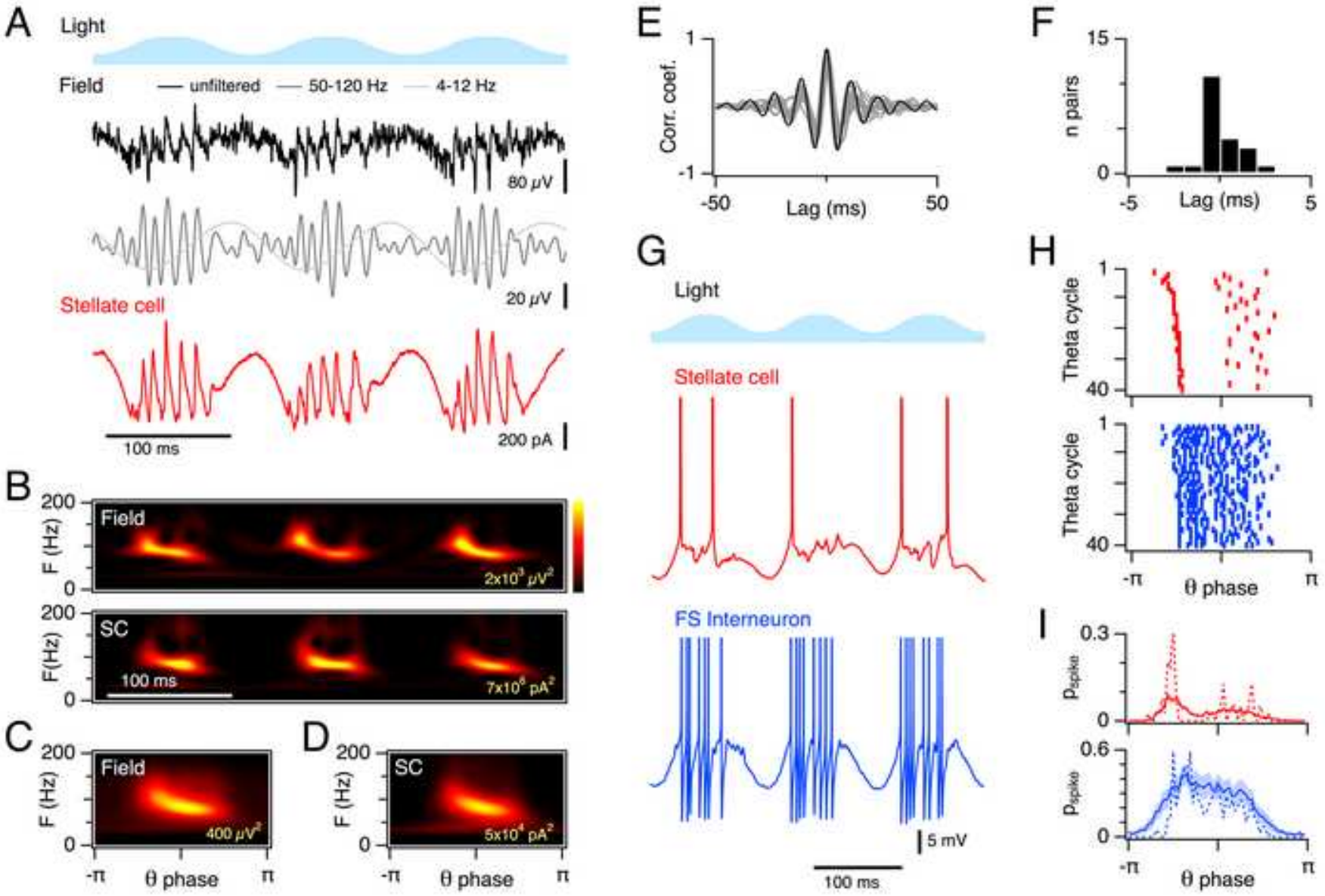

Figure 2

Click here to download high resolution image

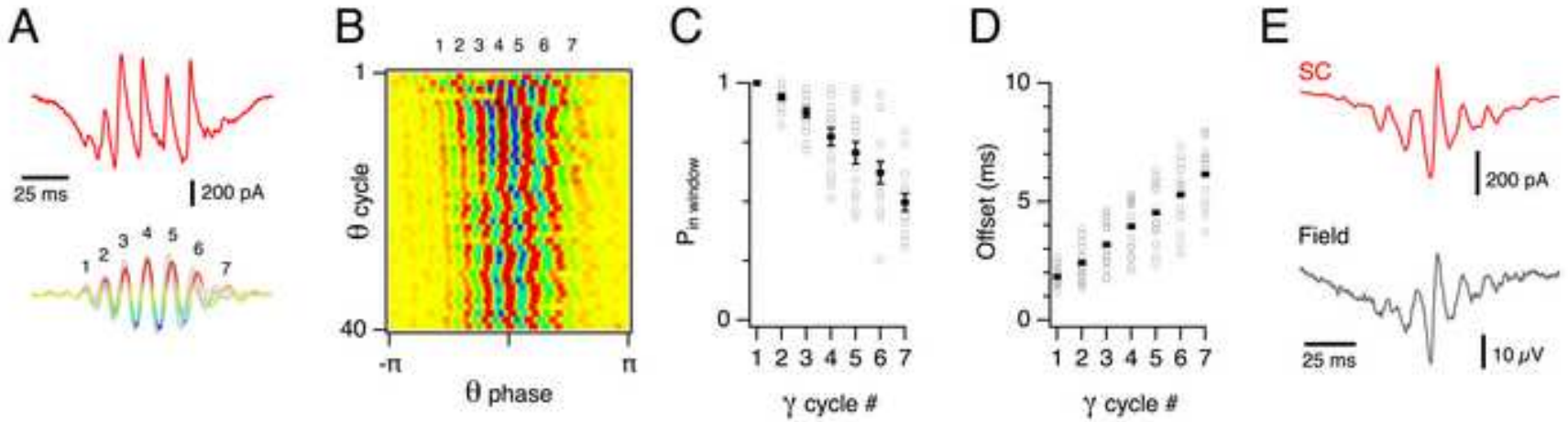

Figure 3

Click here to download high resolution image

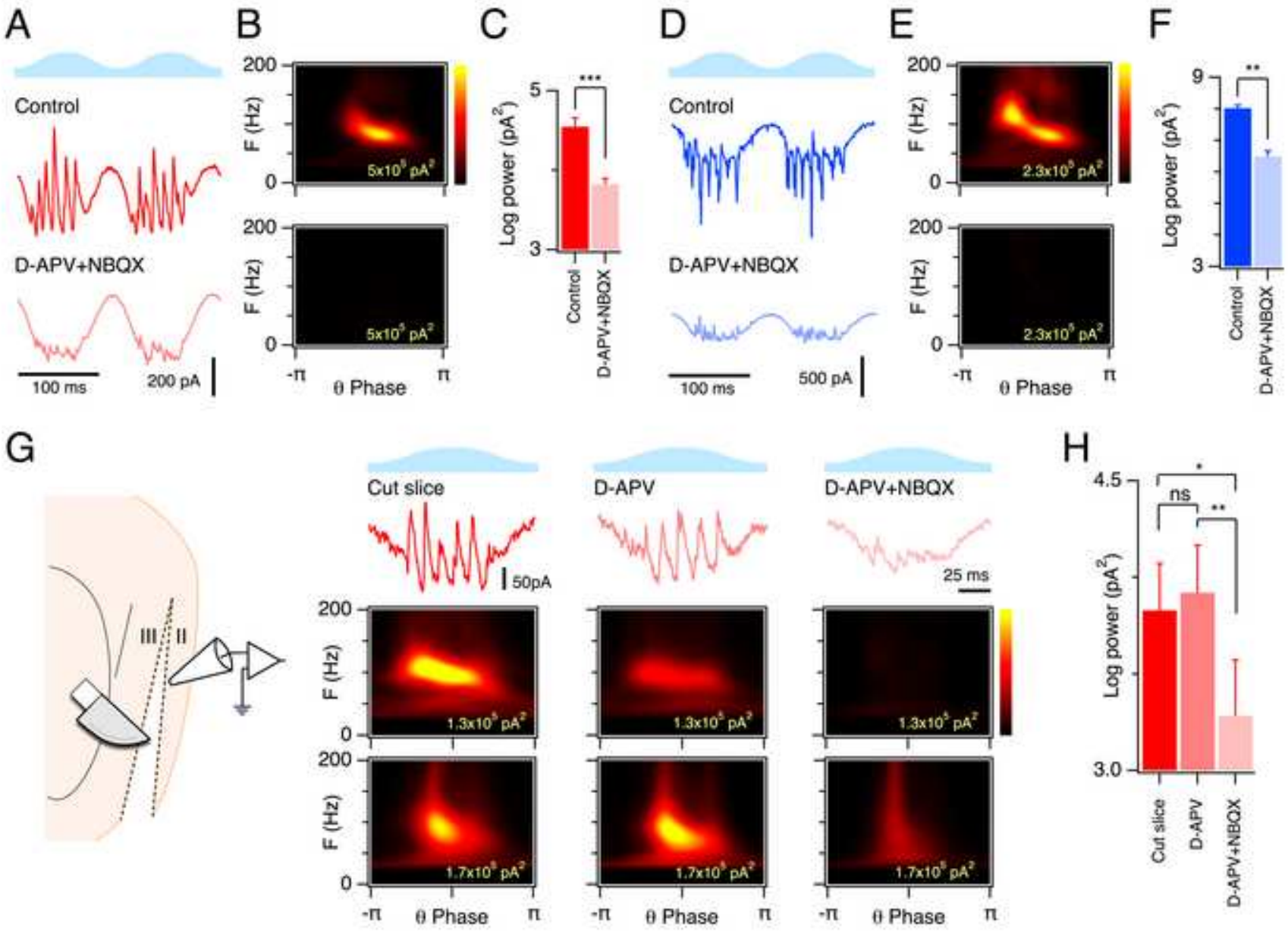

Figure 4
Click here to download high resolution image

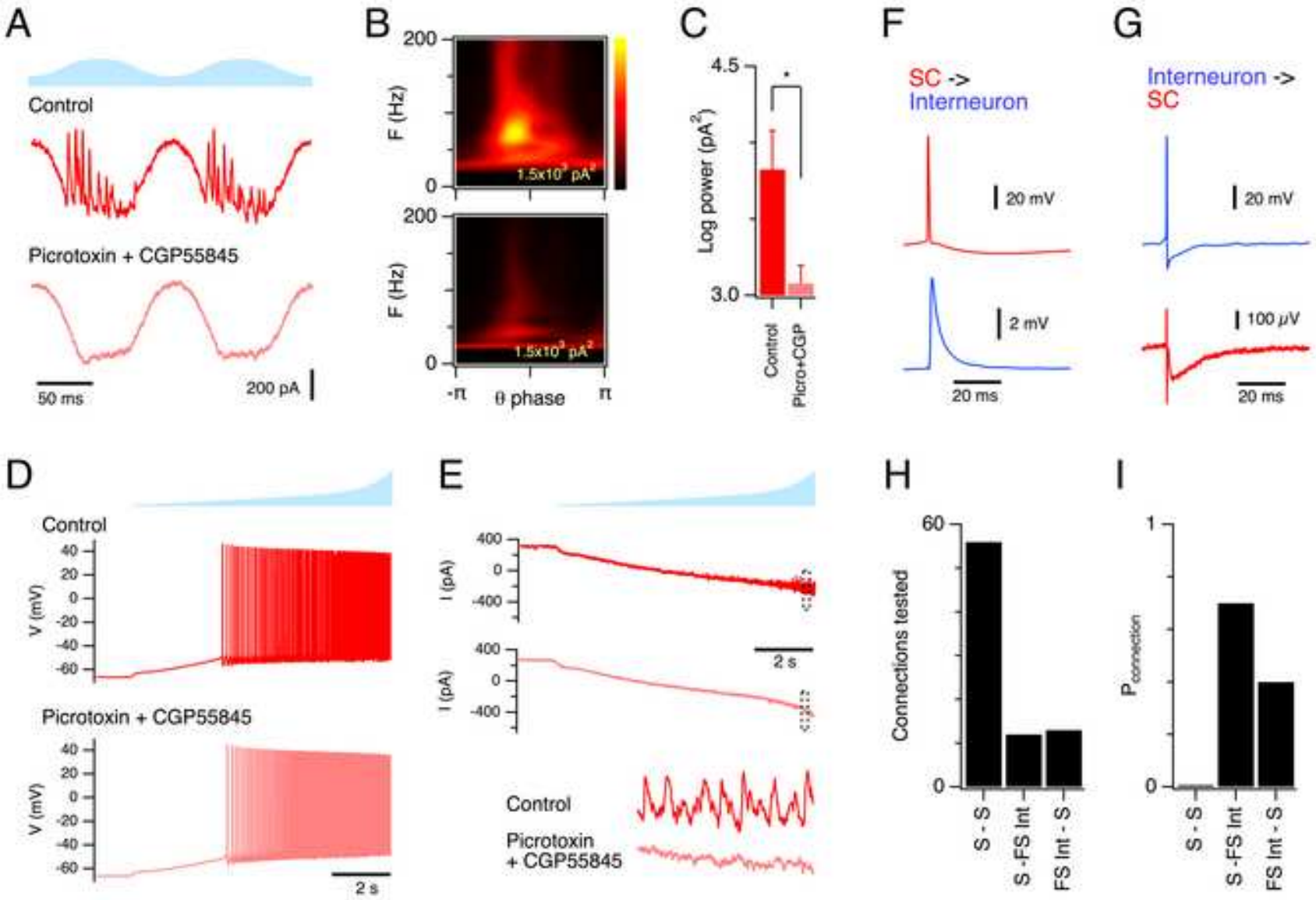

Figure 5
Click here to download high resolution image

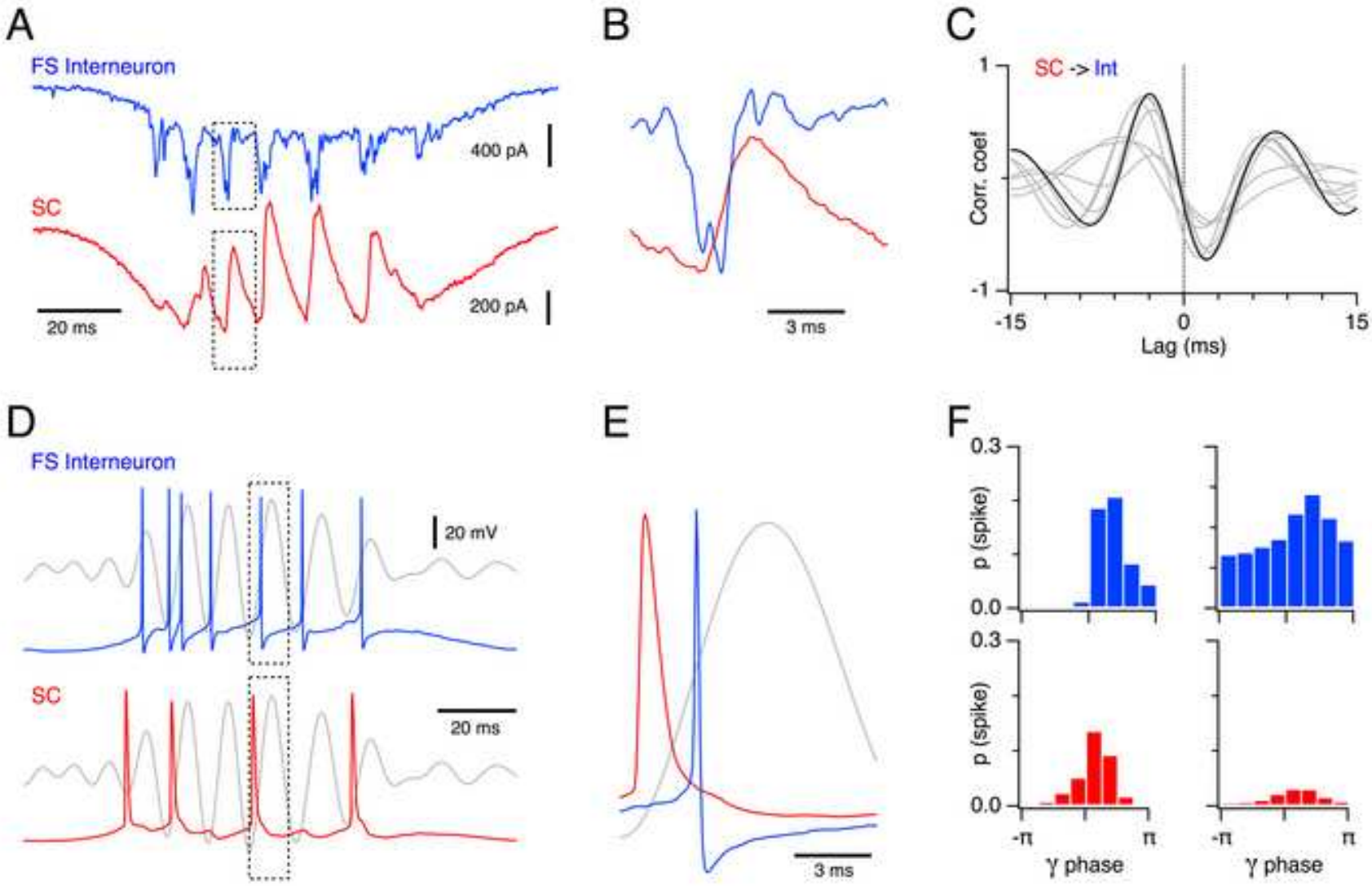

Figure 6

Click here to download high resolution image

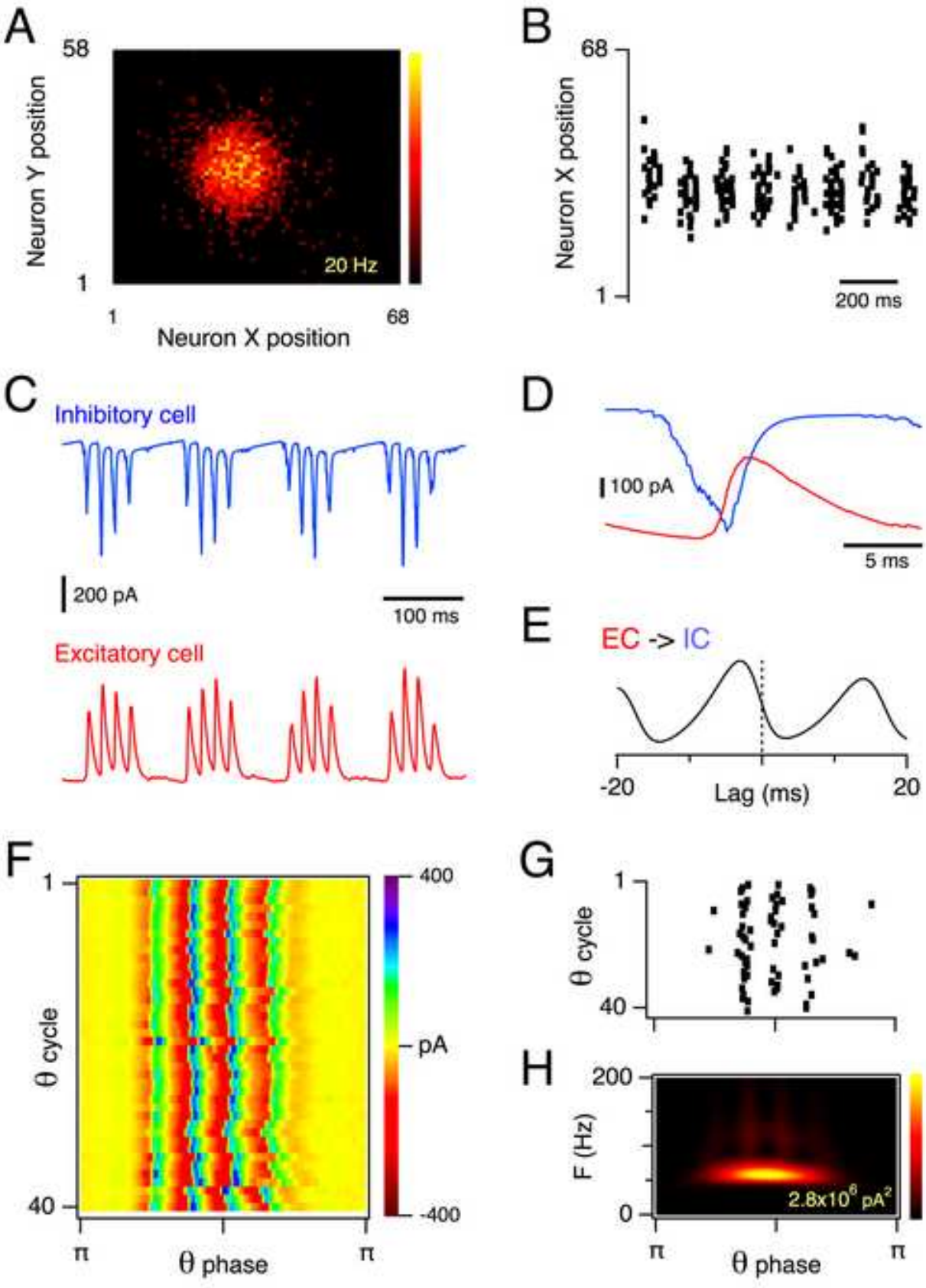

Figure 7
Click here to download high resolution image

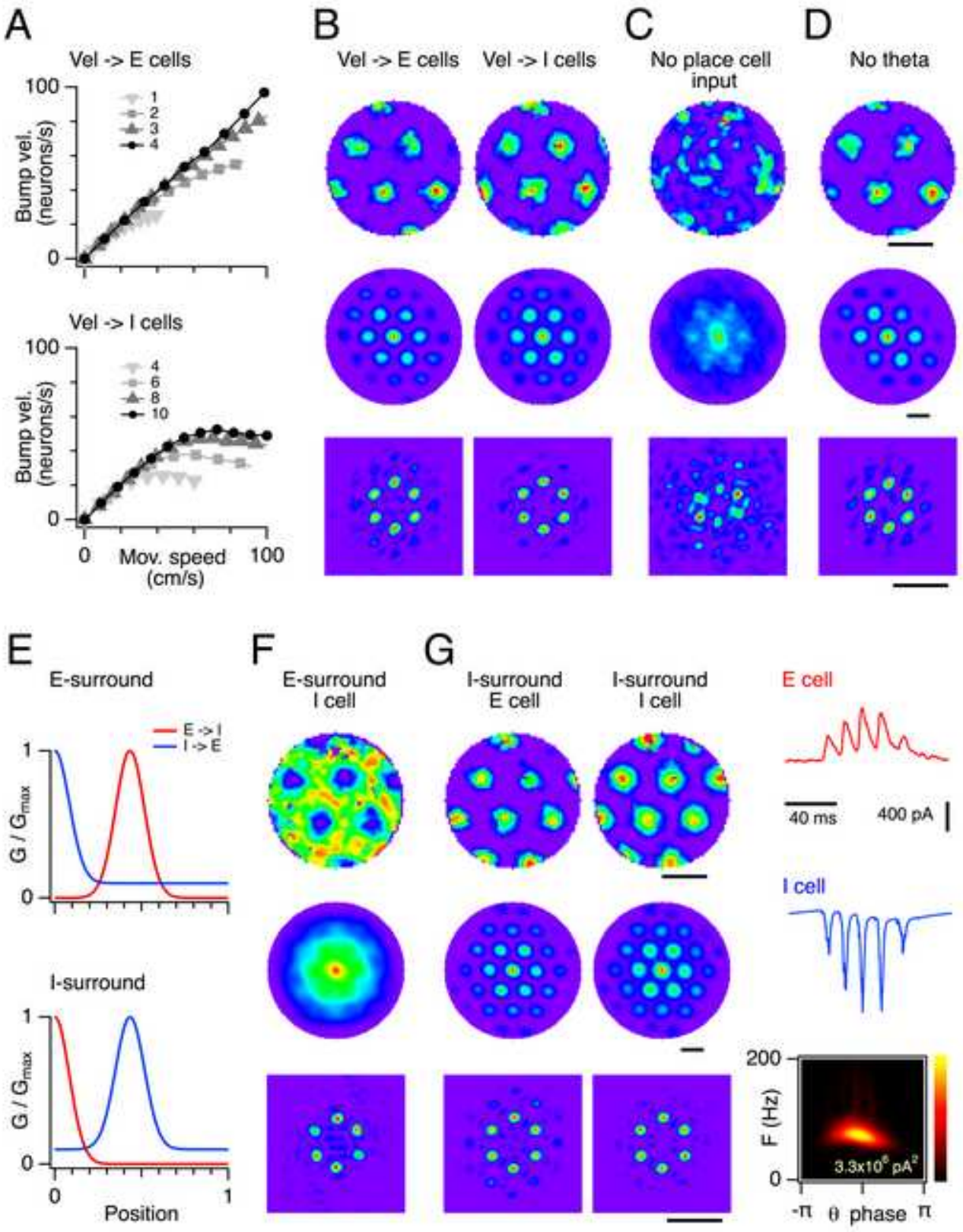

Figure 8

Click here to download high resolution image

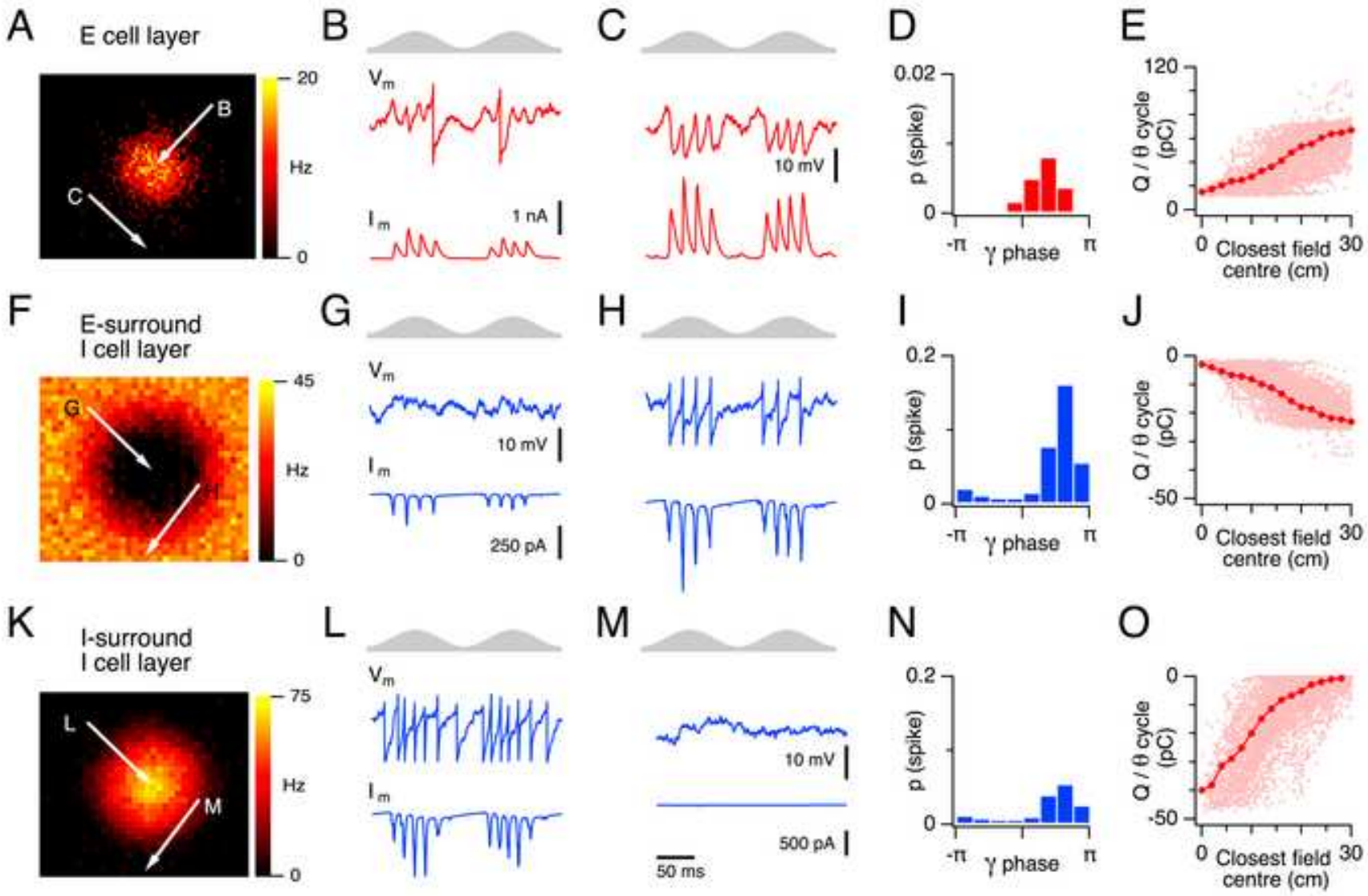

Feedback inhibition enables theta-nested gamma oscillations and grid firing fields

Hugh Pastoll, Lukas Solanka, Mark C.W. van Rossum, Matthew F. Nolan

SUPPLEMENTAL DATA

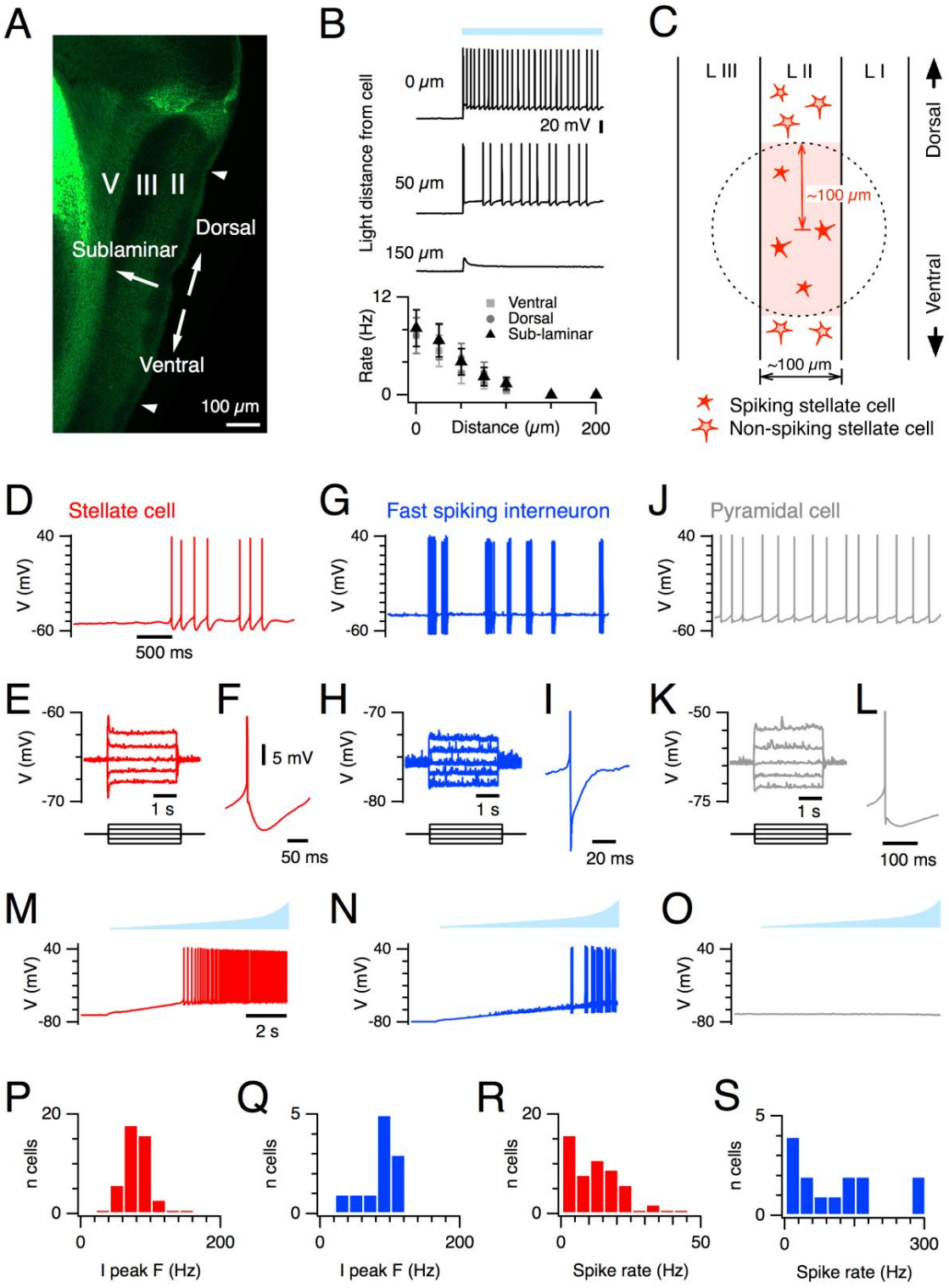

Figure S1

Figure S1. Optogenetic activation of neurons in layer II of the MEC
(A) YFP signal indicating location of neurons expressing ChR2 in a sagittal section of a brain from a Thy1-Chr2-YFP mouse. Expression is in cells from layer II of the MEC, but not adjacent layer III. Arrowheads indicate dorsal (upper) and ventral (lower) borders of the MEC. Lamina II, III and V of the MEC are indicated by Roman numerals.
(B) Light induced depolarization of a layer II stellate cell from a Thy1-Chr2-YFP mouse. In the upper trace the recorded neuron is in the centre of the illuminated field. In the lower traces the recorded neuron is moved by the indicated distance in a dorsal direction away from the centre of the illuminated region. Horizontal bar corresponds to 470 nm light. The mean frequency of action potentials fired by SCs is plotted as a function of distance from the centre of the illuminated region in dorsal, ventral and sub-laminar direction (lower). Similar functional experiments indicated absence of ChR2 from neurons in layer III of the MEC. This is consistent with the absence of YFP from layer III in (A).
(C) Because the full dorsal-ventral extent of the MEC is greater than 2 mm, the restricted size of the illuminated region (approximately 100 μm diameter) results in restricted subsets of layer II neurons being activated.
(D) Representative example of action potentials fired by a stellate cell during injection of constant positive current. The slow (approximately 10 Hz) clustered patterns of action potentials are a distinct property of stellate cells (Pastoll et al., 2012a).
(E) Responses of the stellate cell in (D) to a series of current steps (-80 to 80 pA). The rapid sag like response is a distinctive property of stellate cells.
(F) Action potential afterhyperpolarization from the cell in (D-E) is slower than that of a fast spiking interneuron and has larger amplitude than that of a typical pyramidal cell.
(G-I) Representative data from a FS interneuron as for (D-F). The FS interneuron fires action potential bursts at very high frequency (G), has a hyperpolarized resting membrane potential and minimal sag response (H) and short, large amplitude after-hyperpolarization (I).
(J-L) Representative data from a pyramidal cell as for (D-F) and (G-I). Pyramidal cells fire action potential trains at low frequencies without pauses (J), have a small amplitude sag response (K), a small amplitude afterhyperpolarization (L).
(M-O) In layer II of the MEC from Thy1-ChR2-YFP mice stellate cells (n = 235/235) and fast spiking interneurons (n = 41/41) are depolarized by light, but pyramidal neurons are not (n = 0/11).
(M) Membrane depolarization (lower) of an SC by a ramped light stimulus (upper) triggers action potential firing.
(N) FS interneurons also fire action potentials in response to optical stimulation.
(O) Pyramidal cells are not depolarized by light activation.
(P-S) Population distribution of oscillation and action potential frequencies
(P) Histogram of the frequency of the peak in the scalogram of membrane current recorded from stellate cells during theta frequency stimulation of layer II (see Figure 1C).
(Q) As for (P) except data is for fast spiking interneurons.
(R) Histogram of the mean spike rate of stellate cells during theta frequency stimulation (see Figure 1G-H).
(S) As for (R) except data is for fast spiking interneurons.

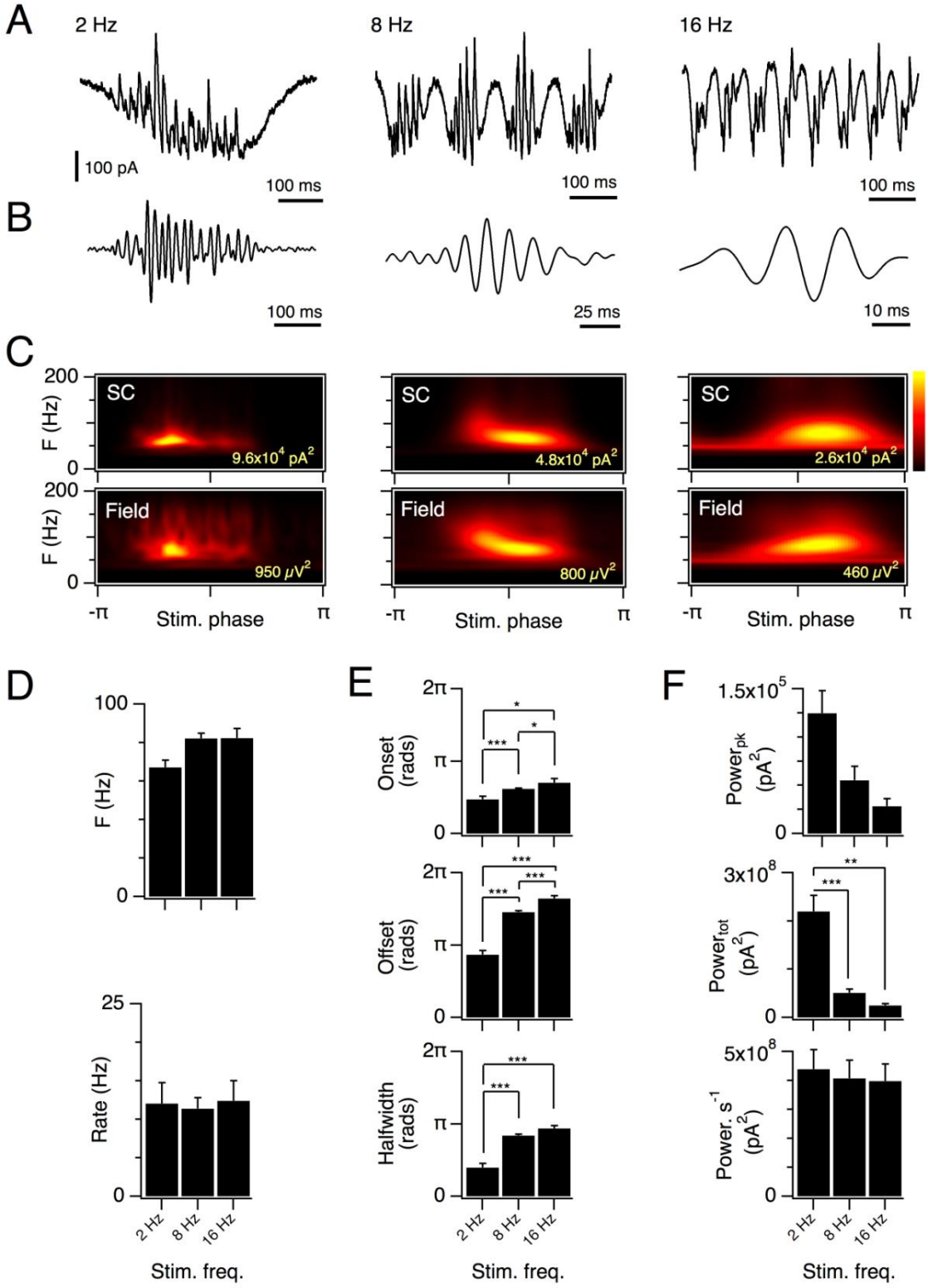
A
2 Hz
8 Hz
16 Hz
100 pA
100 ms
100 ms
100 ms
B
100 ms
25 ms
10 ms
C
200
F (Hz)
0
SC
9.6x10^4 pA^2
4.8x10^4 pA^2
2.6x10^4 pA^2
Field
950 μV^2
800 μV^2
460 μV^2
-π
Stim. phase
π
D
100
F (Hz)
0
25
Rate (Hz)
0
2 Hz
8 Hz
16 Hz
Stim. freq.
E
2π
π
0
Onset (rads)
Offset (rads)
Halfwidth (rads)
*
***
F
1.5x10^5
Power_pk (pA^2)
3x10^8
Power_tot (pA^2)
**
5x10^8
Power. s^-1 (pA^2)

Figure S2

Figure S2. Responses to optical stimulation at 2, 8, and 16 Hz
(A) Examples of membrane currents recorded from SCs in response to optical stimulation at different frequencies. The number of gamma oscillations per stimulus cycle depended on the frequency of the optical input ($p < 10^{-9}$, ANOVA), and differed significantly between responses to 8 Hz and 2 Hz stimulation ($p < 10^{-9}$, t-test) and between responses to 8 and 16 Hz stimulation ($p < 10^{-9}$, t-test). The total number of gamma cycles per second of stimulation also depended on the frequency of the optical input ($p < 10^{-9}$, ANOVA), and differed significantly between responses to 8 Hz and 2 Hz stimulation ($p = 0.0003$, t-test) and between responses to 8 and 16 Hz stimulation ($p < 10^{-9}$, t-test).
(B) A single stimulus cycle from each trace in (A). The traces are band pass filtered and the time base modified so that activity is shown relative to the scale of the driving stimulus.
(C) Scalograms for membrane currents (upper) and field potentials (lower) for the example recordings in (A-B).
(D) Frequency of the maximum power (upper) ($n = 6, 45, 4$, $p = 0.12$, ANOVA) and action potential firing rate (lower) ($n = 8, 51, 8$, $p = 0.99$, ANOVA) in response to stimulation at 2, 8 and 16 Hz.
(E) Phase of onset (upper) $p = 4.6 \times 10^{-6}$ and offset (middle), $p = 10^{-14}$ and half-width $p = 1.9 \times 10^{-11}$, of gamma activity for each stimulation frequency ($n = 6, 45, 4$, ANOVA for all tests).
(F) Peak power (upper) $p = 0.1$, total power (middle) $p = 9.3 \times 10^{-9}$ and power normalized to time $p = 0.99$ (lower) for oscillatory responses to stimulation at each frequency ($n = 6, 45, 4$, ANOVA for all tests). Results of post-hoc t-tests are indicated on each panel, where * is $p < 0.05$, ** is $p < 0.01$, and *** is $p < 0.001$.

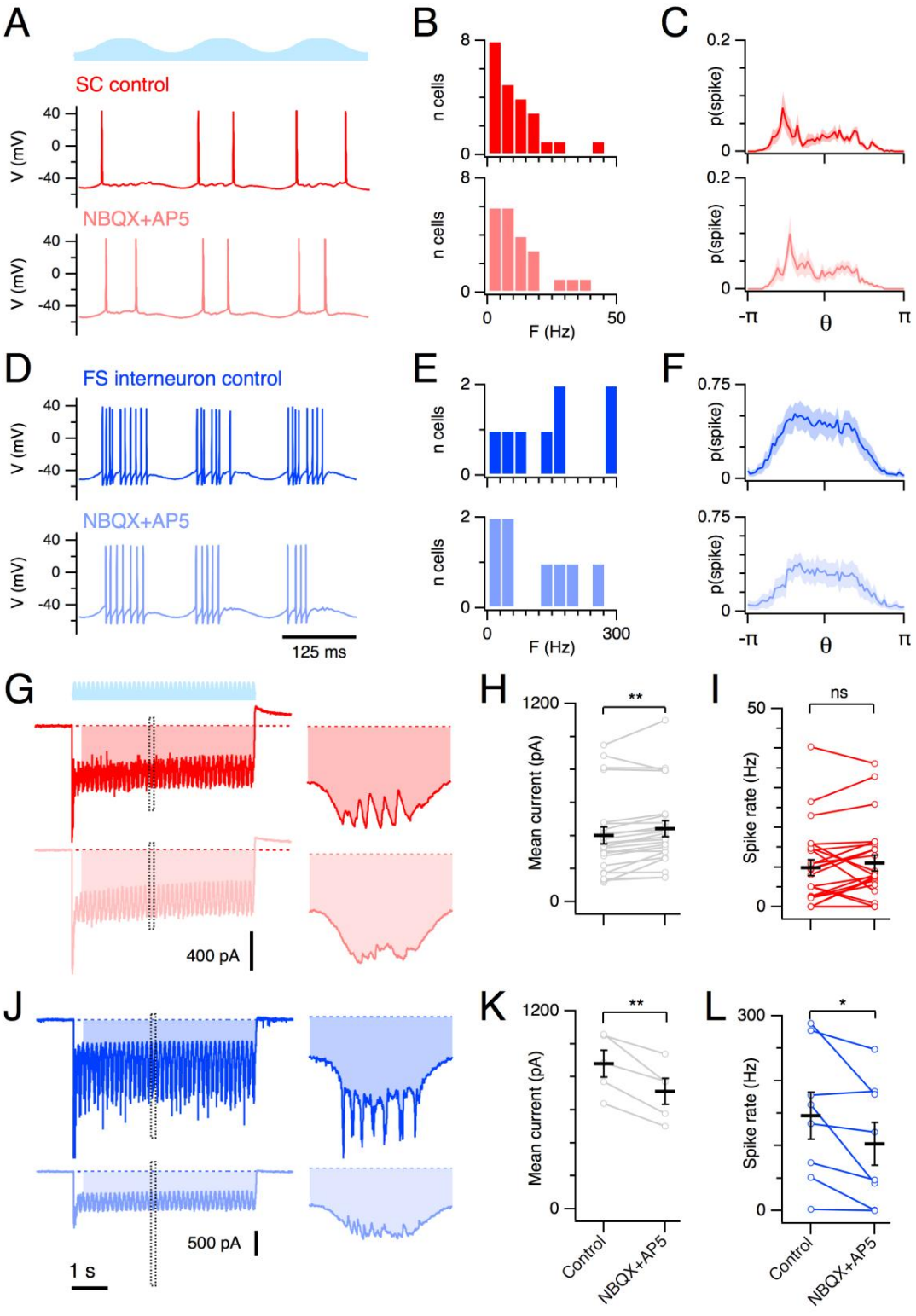
A
SC control
V (mV)
40
0
-40
NBQX+AP5
B
n cells
8
0
F (Hz)
50
C
p(spike)
0.2
-π
θ
π
D
FS interneuron control
125 ms
E
2
300
F
0.75
G
400 pA
H
Mean current (pA)
1200
**
I
Spike rate (Hz)
50
ns
J
500 pA
1 s
K
L
300
*
Control
NBQX+AP5

Figure S3

Figure S3. Action potential firing by SCs and FS interneurons is maintained during block of iGluRs

(A) Example of membrane potential responses of an SC to theta stimulation of layer II (upper trace) in control conditions (middle trace) and during block of iGluRs with NBQX (5 μM) and D-APV (50 μM) (lower trace).

(B) Binned mean firing rate distribution for SCs in each condition ($p = 0.89$, n=24, Kolmogorov-Smirnov test).

(C) Mean distribution of firing probability as a function of theta phase for all SCs. In both conditions firing probability differed as a function of theta phase (18/19 vs 19/19 significant, Kuiper test for uniformity). There was no significant difference between the firing phase of spikes in the two groups ($p = 0.1$, $n = 19$, Moore's test for paired angles).

(D) Example of membrane potential responses of a FS interneuron to theta stimulation of layer II in control conditions (upper trace) and during block of iGluRs with NBQX (5 μM) and D-APV (50 μM) (lower trace).

(E-F) As for (B-C) except data are for FS interneurons (Binned mean firing rate distributions: $n = 8$, $p = 0.6$, Kolmogorov-Smirnov test; Theta phase distribution of firing: 8/8 vs 6/6 significant, Kuiper test, $n = 6$, $p = 0.6$; Moore's test for paired angles).

(G) Example of membrane current responses of an SC to theta frequency activation of ChR2 in control conditions (upper) and after block of iGluRs with NBQX (5 μM) and D-APV (50 μM) (lower traces).

(H) Change in mean membrane current of SCs ($p = 0.0014$, $n = 23$, paired t-test).

(I) Change in mean firing rate of SCs in (A-C) ($p = 0.28$, $n = 24$, paired t-test).

(J-K) As for (G-H) except data are for fast spiking interneurons ($p = 0.007$, $n = 5$, paired t-test).

(L) Change in mean firing rate for interneurons in (D-F), ($p = 0.04$, $n = 8$, paired t-test).

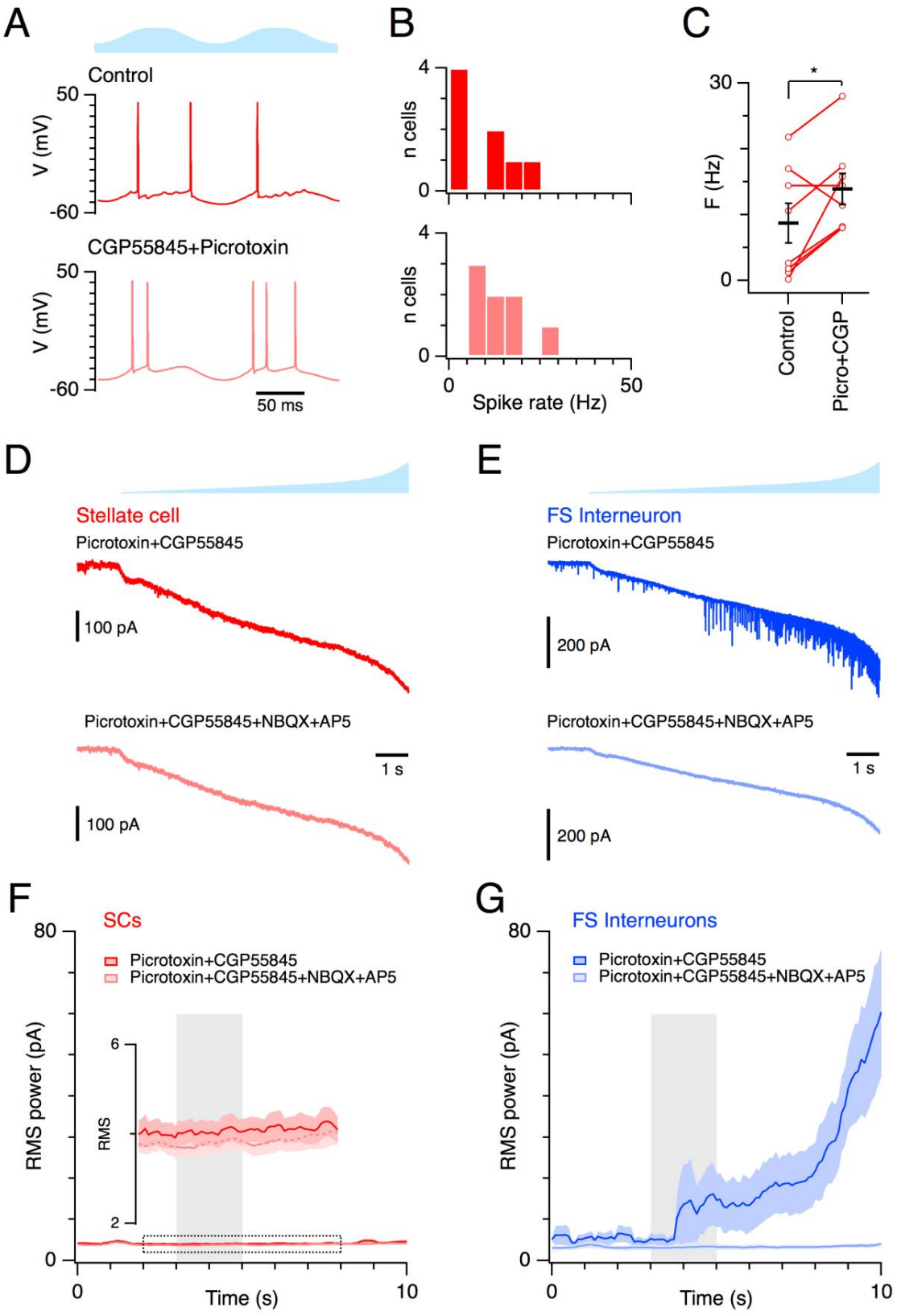
A
Control
V (mV)
50
-60
CGP55845+Picrotoxin
50 ms
B
n cells
4
0
Spike rate (Hz)
50
C
F (Hz)
30
0
*
Control
Picro+CGP
D
Stellate cell
Picrotoxin+CGP55845
100 pA
Picrotoxin+CGP55845+NBQX+AP5
1 s
E
FS Interneuron
200 pA
F
SCs
Picrotoxin+CGP55845
Picrotoxin+CGP55845+NBQX+AP5
RMS power (pA)
RMS
6
2
80
Time (s)
10
G
FS Interneurons

Figure S4

Figure S4. Block of synaptic inhibition has little effect on SC firing rate and does not reveal excitatory input to SCs

(A) Examples of action potentials fired by an SC during theta frequency network stimulation (upper) in control conditions (middle) and during block of GABA receptors with picrotoxin and CGP55845 (lower).

(B) Binned mean spike frequency in control conditions (upper) and during block of GABA receptors (lower) ($p = 0.26$, $n = 8$, Kolmogorov-Smirnov test).

(C) Change in mean spike frequency for individual SCs ($p = 0.046$, $n = 8$, paired t-test).

(D-E) Example responses of an SC (D) and a fast spiking interneuron (E) to a ramped light stimulation (upper traces). Responses are recorded first in the presence of extracellular picrotoxin (50 μM) and CGP55485 (1 μM) to block $GABA_A$ and $GABA_B$ receptors respectively (middle traces). Responses were then recorded from the same neurons after addition of NBQX (5 μM) and D-APV (50 μM) to the extracellular solution to also block AMPA and NMDA ionotropic glutamate receptors.

(F-G) Plot of the root mean square (RMS) power (11 cells, ± SEM indicated by shaded area) as a function of time during the light stimulus. The grey shaded area indicates the times of first spikes fired by SCs recorded in current-clamp configuration in response to the same light ramp stimulus. The holding potential was -70 mV. To evaluate the effects of light level and recording condition we used MANOVA with factors for drug condition and irradiance. We find that for recording from SCs there is no effect of drug condition ($P = 0.18$) or irradiance ($P = 0.15$) and no interaction between the factors ($P = 0.96$). Thus, while excitatory synaptic responses are clearly manifest as an increase in RMS power in the recordings from interneurons (G), the data from 11 SCs do not reveal evidence of synaptic responses (F).

Taking the conservative estimate that ~200 stellate cells are driven to spike during light ramps in each slice experiment (see Supplemental Figure 1B-C and Supplemental Experimental Procedures) and considering the data from these 11 experiments, this gives a total of 2200 tested potential connections. Rounding down to 2000 tested potential connections, and then accounting for possible sampling variability (see Supplemental Experimental Procedures), gives 95 % confidence that the maximum probability of direct stellate to stellate connections is 0.0015 (or 1:667). This limit on connectivity is consistent with the fact that SC-SC connections are not detectable in paired recordings between SCs (Figure 4) and is in contrast to the probability of connections between SCs and interneurons, which is greater than 1 in 3 in either direction (Figure 4).

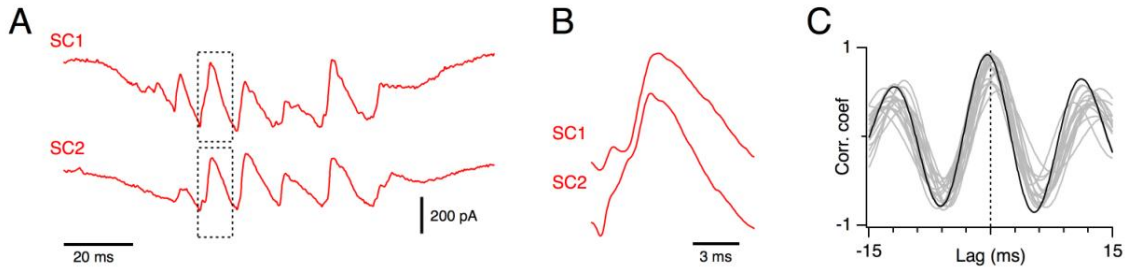

Figure S5. Synchronization of gamma frequency input to stellate cells by theta stimulation

(A) Example of membrane currents recorded simultaneously from two stellate cells during a single epoch of theta stimulation.

(B) Compound inhibitory synaptic currents indicated in (A) are shown on an expanded time scale.

(C) Cross-correlation between membrane currents from simultaneously recorded pairs of stellate cells during theta frequency stimulation. The correlation for the example in (A-B) is indicated with a dark line and other cell pairs are indicated with grey lines. The average maximum correlation was 0.71 ± 0.04 and the lag was 0.077 ± 0.16 ms.

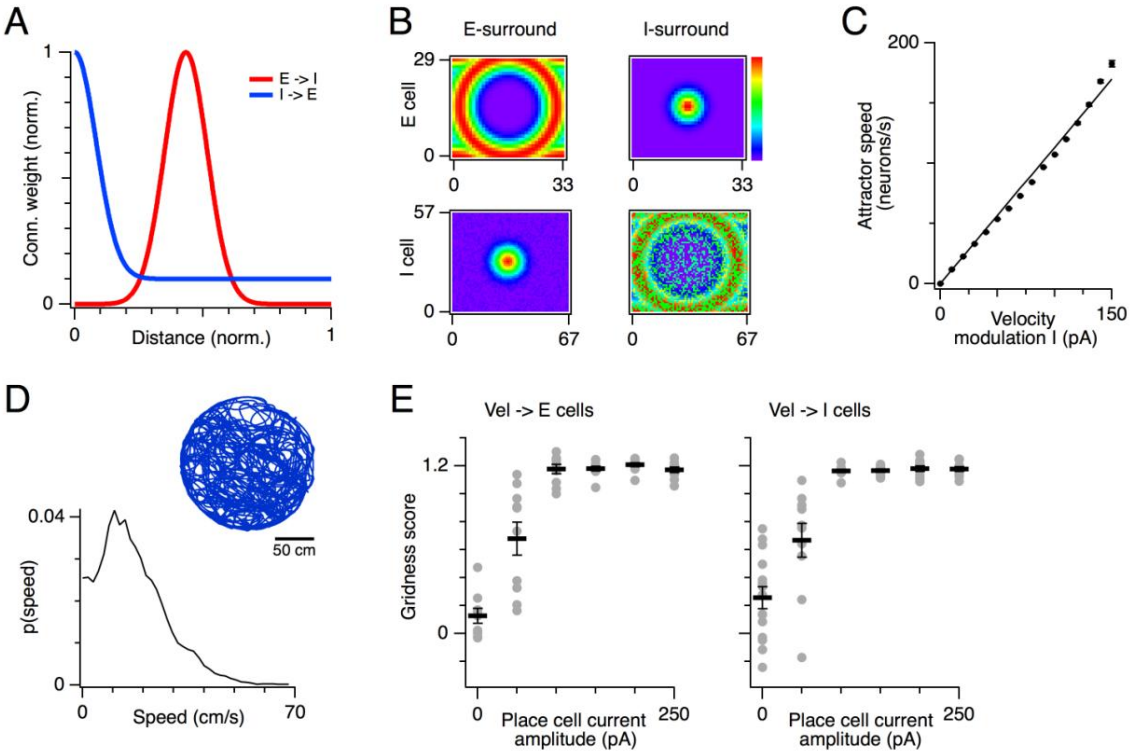

Figure S6. Attractor network model

(A) Normalized connection weights plotted as a function of distance for inputs from excitatory cells onto inhibitory interneurons (red) and from inhibitory interneurons onto excitatory cells (blue). Full details of implementation are described in the Experimental Procedures.

(B) Plots illustrate normalized connection strengths (red strong, purple weak) onto each interneuron in a 34 x 30 matrix from an excitatory neuron at the centre of the sheet (upper) and onto each of a 68 x 58 matrix of excitatory neurons from an interneuron at the centre of the sheet (lower) for the E-surround (left) and I-surround (right) network configurations.

(C) Attractor speed plotted as a function of the velocity modulation current (I_{vel} in Experimental Procedures). The slope of this relationship is a fixed property of a network. Grid firing fields of different spacing can be achieved by modifying the network to adjust the slope, or by changing the relationship between movement speed and the velocity modulation current.

(D) Trajectory (upper) and speed distribution (lower) for the velocity input used for simulation of movement in a circular arena.

(E) Gridness score plotted as a function of the amplitude of the place cell input for networks in which the velocity input targets excitatory cells (left) or inhibitory cells (right).

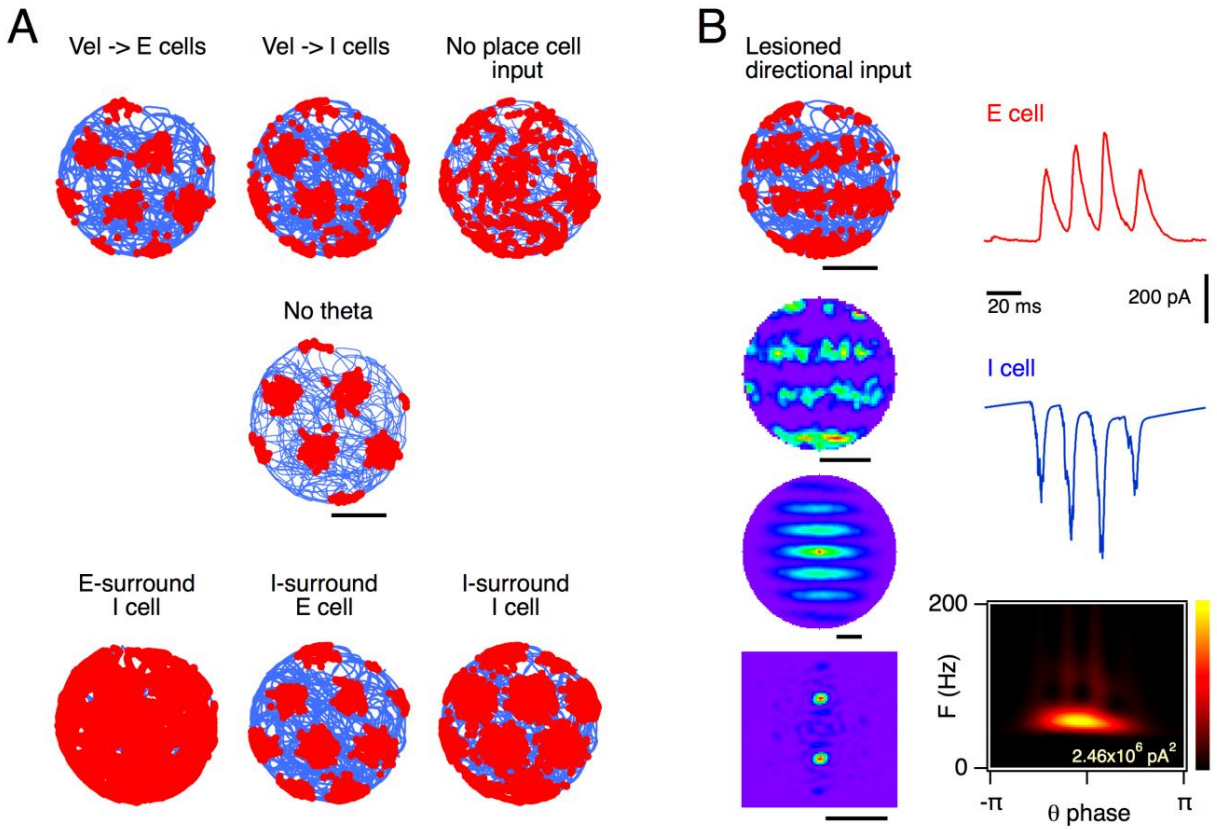

Figure S7. Spike locations for model configurations and band cell theta-nested gamma.
(A) Locations of action potential firing (red dots) and simulated trajectory (blue lines) for the example neurons in Figure 7(B-D and F-G).
(B) Examples of action potential location (left row 1), smoothed firing rate plot (left row 2), spatial autocorrelogram (left row 3) and 2D Fourier spectrogram (left row 4) for a neuron in a network with all but one direction of velocity input removed. Neurons in this network appear as band cells. This network configuration also generates theta-nested gamma activity illustrated by recordings of synaptic currents during a single theta cycle from an excitatory cell (upper right), inhibitory cell (middle right) and the scalogram of the synaptic activity as a function of theta cycle phase for the synaptic currents onto an excitatory cell (lower right). Scale bars are 60 cm for the rate and autocorrelation plots and 4 m^{-1} for the spatial Fourier transforms.

SUPPLEMENTAL EXPERIMENTAL PROCEDURES

Electrophysiological recordings

All experiments used adult (7 - 9 week old) mice from Thy1-ChR2-YFP line 18 (stock number 007612 from The Jackson Laboratory) (Arenkiel et al., 2007). Sagittal brain slices were prepared and whole-cell patch-clamp recordings made from neurons in layer II of the MEC as described previously (Garden et al., 2008; Pastoll et al., 2012b). The slices include all layers and the full dorsal-ventral extent of the MEC. For preparation of slices the cutting solution had composition (mM): NaCl 86, NaH_2PO_4 1.2, KCl 2.5, $NaHCO_3$ 25, Glucose 25, Sucrose 75, $CaCl_2$ 0.5, $MgCl_2$ 7. For maintenance of slices and for making recordings the extracellular solution had composition (mM): NaCl 124, NaH_2PO_4 1.2, KCl 2.5, $NaHCO_3$ 25, Glucose 20, $CaCl_2$ 2, $MgCl_2$ 1. For patch-clamp recordings the intracellular solution had composition (mM): K Gluconate 130; KCl 10, HEPES 10, $MgCl_2$ 2, EGTA 0.1, Na_2ATP 2, Na_2GTP 0.3 NaPhosphocreatine 10. In patch-clamp recordings an experimentally measured liquid junction potential of 12.9 mV was not corrected for.

SCs were identified by their characteristic large sag response to positive and negative current steps and by their generation of distinct clustered patterns of action potentials (Garden et al., 2008; Pastoll et al., 2012a). The excitatory nature of neurons meeting these criteria is confirmed by exclusively excitatory synaptic responses recorded from connected postsynaptic neurons (Figure 4F). FS interneurons were identified by their large cell bodies prior to recording, by the high frequency at which they fire action potentials during depolarizing current steps and by their short action potentials which are followed by a large and brief after-hyperpolarization (Figure S1)(Jones and Buhl, 1993). The inhibitory nature of neurons meeting these criteria is confirmed by exclusively inhibitory synaptic responses recorded from connected postsynaptic neurons (Figure 4G).

Illumination for activation of ChR2 was from a 470 nM collimated LED (Thorlabs) introduced through the epifluorescence port of the microscope (Olympus BX-51) and focused onto the slice from above (Figure S1). The irradiance of the LED (up to a maximum of ~22 mW/mm^2) was controlled by custom analogue voltage commands. The region of neurons activated by light had a radius of approximately 100 μm and depth greater than 100 μm (Figure S1C). Voltage-clamp experiments were performed with a holding potential of -50 mV unless otherwise indicated and series resistance of ≤ 25 MΩ

which was compensated by ≥ 70%. Current-clamp experiments were carried out with series resistance ≤ 30 MΩ, and with bridge-balance and pipette capacitance neutralization applied. Pharmacological agents were bath applied to the whole slice. Pharmacological agents were obtained from Abcam and had final concentration in the standard extracellular solution as follows (μM): NBQX 5, AP5 50, Picrotoxin 50, CGP55845 1.

Attractor network model

A network of exponential integrate and fire neurons (Fourcaud-Trocme et al., 2003) was implemented using the Brian simulator (Goodman and Brette, 2008). For each neuron:

$$C\frac{dV_m}{dt} = g_L(E_L - V_m) + g_{ahp}(E_{ahp} - V_m) + g_L\Delta_T \exp\left(\frac{V_m - V_t}{\Delta_T}\right) + I_{syn} + I_{ext}$$

Where C is the membrane capacitance, g_L is a leak conductance, E_L is the equilibrium potential for the leak conductance and therefore sets the resting membrane potential, V_m is the membrane potential, g_{ahp} is a conductance that mediates the action potential after-hyperpolarization, E_{ahp} is the equilibrium potential for g_{ahp}, Δ_T determines the sharpness of the action potential rise phase,V_t is the threshold for initiation of an action potential, I_{syn} is the local synaptic current and I_{ext} is an external current.

SCs were modeled as excitatory neurons with average time constant (C/g_L) of 9.3 ms drawn from a uniform distribution with standard deviation 0.31 ms, a resting membrane potential of -68.5 mV, a spike initiation threshold of -50 mV and Δ_T of 0.4 mV. Following each action potential the membrane potential was reset to -68.5 mV. After a spike, g_{ahp} was set to 5 nS and decayed with a time constant of 10 ms. FS interneurons were modeled as inhibitory neurons with time constant of 7 ms, resting membrane potential -60 mV, spike initiation threshold -45 mV and Δ_T of 0.4 ms. Following each action potential the membrane potential was reset to -60 mV, with g_{ahp} increased by 22 nS and then decaying with a time constant of 7.5 ms. The equilibrium potential for the current through g_{ahp} was -80 mV in SCs and -60 mV in FS interneurons. In both neuron types g_L = 22.73 nS.

Excitatory synaptic conductances were modeled as the sum of fast AMPA and slower

NMDA components, with the peak NMDA conductance equal to 2 % of the peak AMPA conductance. Both components activate instantaneously and have decay kinetics described by a single exponential, with decay time constants of 1 ms (AMPA) and 100 ms (NMDA). The voltage dependence of the NMDA component was not considered. Inhibitory synaptic conductances ($GABA_A$) were modeled as a difference of exponentials with rise time constant of 0.1 ms and a decay time constants of 5 ms. Equilibrium potentials were as follows: AMPA 0 mV, NMDA 0 mV, $GABA_A$ -75 mV.

Each neuron received an external current source (I_{ext}) composed of (i) constant background activation (I_{const}), (ii) theta modulated current simulated as a cosine function (I_{theta}), (iii) velocity modulated current (I_{vel}), (iv) hippocampal place field input (I_{place}):

$$I_{ext} = I_{const} + I_{theta} + I_{vel} + I_{place}$$

The activity bump was initialized by applying place cell input (see below) of amplitude 300 pA during the first 100 ms of simulation. To simulate noise in the network, independent Gaussian distributed current was injected to give a 2 mV standard deviation in the resting membrane potential of each neuron. For excitatory cells and interneurons I_{const} = 300 pA and 200 pA respectively, and I_{theta} is a cosine function with frequency 8 Hz and amplitude 187.5 pA and 12.5 pA respectively for the E-surround configuration, and 325 pA and 25 pA for the I-surround configuration. Velocity and place inputs are described in more detail below. In the basic version of the model depicted in Figure 6 interneurons have I_{vel} and I_{place} set to zero.

Network topology and Connectivity. The network consisted of 68 x 58 excitatory cells and 34 x 30 interneurons uniformly distributed on a twisted torus with normalized X vs Y dimensions of 1 vs 0.5 x √3 (Guanella et al., 2007). The numbers of neurons used in the model are considerably lower than estimates of the total numbers of cells in layer II of the MEC (Gatome et al., 2010). The torus dimensions are normalized in order to map both excitatory and inhibitory populations to a common space. Connections from excitatory to inhibitory cells used AMPA and NMDA type conductances and their topography in the E-surround configuration follows a ring-like organization (Figure S6A-B) with the conductance of a connection from excitatory neuron j to inhibitory neuron i (W_{ij})

determined by the following equations:

$$W_{ij} = G_{exc} \exp\left(\frac{-(d(i,j,C) - \mu_{exc})^2}{2\sigma_{exc}^2}\right)$$
$$d(i,j,C) = |\mathbf{u}_i - \mathbf{u}_j - C\mathbf{e}_p|$$

where d is the distance apart on the twisted torus of neurons i and j and includes an offset, μ_{exc} is the center of the profile, σ_{exc} is its width and G_{exc} is the maximal value of the synaptic weight profile. $\mathbf{u_i}$ and $\mathbf{u_j}$ are vectors representing the positions of both neurons and $\mathbf{e_p}$ is a unit vector in the direction of preferred movement (cf. Velocity modulation). C specifies the amount of the excitatory profile offset and was set to a value of 4 when velocity modulated inputs targeted stellate cells and 0 when the velocity inputs targeted FS interneurons.

In the E-surround configuration of the network the topography of inhibitory to excitatory connection weights (U_{ij}) had a Gaussian profile (Figure S6A-B and Figure 7E):

$$U_{ij} = G_{inh} \exp\left(\frac{-d(i,j,0)^2}{2\sigma_{inh}^2}\right)$$

where σ_{inh} is the width of the profile and G_{inh} = 2.12 nS is the maximal value of the synaptic weight profile and d is the distance specified in the equation above, in which C was set to 0 for velocity inputs targeting stellate cells and 10 for the velocity inputs targeting FS interneurons. In addition, each interneuron sends inhibitory synapses to every SC with a fixed probability of connection, set to 0.4 in all simulation experiments, and peak synaptic conductance of 68.6 pS for the E-surround and 306.4 pS for the I-surround condition respectively (FigureS6A-B). Figure S6B illustrates the outgoing synaptic weights of an excitatory neuron and an interneuron in the middle of the torus. In the I-surround configuration, the topography of the excitatory to inhibitory connections followed the Gaussian profile and G_{exc} set to 1.14 nS, while the connections from inhibitory to excitatory neurons followed the ring-like organization, in which G_{inh} was set to 392 pS.

Velocity modulation. In order to perform path integration in the model, and thus generate grid-like firing fields, the activity in the network must propagate along the direction of the simulated movement of the animal (Fuhs and Touretzky, 2006; Guanella et al., 2007; McNaughton et al., 2006). This is achieved by shifting the centre of the synaptic profile of neurons in one of the populations (excitatory or inhibitory), in the direction of preferred movement. Each neuron is assigned a directional vector from a group of four directions (up, down, left, right) and its outgoing synaptic weight profile is shifted by a predefined constant (cf. $\mathbf{e_p}$ in equations above). During simulated movement of the animal, the velocity modulated current injected into the neuron is computed as follows:

$$\begin{aligned} I_{vel}(t) &= C_v \mathbf{v}(t) \cdot \mathbf{e}_p \\ C_v &= \frac{N_x}{aG} \end{aligned}$$

where **v** is the velocity vector during the simulated movement, $\mathbf{e_p}$ is the unit vector pointing to the preferred direction of bump activity propagation, N_x is the horizontal size of the torus, G is spacing between grid field peaks (cm) and a is the slope of the linear fit to the relationship of bump speed and injected velocity modulated current (Figure S6C). To evaluate spatial representation by the network during exploration in an arena, 15-20 minutes of movement was simulated. At each time point in the simulation the velocity vector was estimated as a forward difference of published positional data (Hafting et al., 2005). The tracking data was corrected for a discontinuity at about 600 s and low pass filtered to remove tracking noise and glitches, while still retaining the original range of velocities and trajectories (Figure S6D).

Place cell input. Unless otherwise stated, all the simulations contain an allothetic input from place cells. This is because while attractor networks modeled with rate coding neurons in the absence of noise show little drift, introduction of action potential firing and noise in the network inevitably leads to slow drift in the state of the network. Consistent with this assumption, grid fields are abolished when hippocampal input to the MEC is lesioned (Fyhn et al., 2004). In the simulations we describe here the synaptic strengths of place cell inputs were predefined rather than being acquired through learning (Guanella et

al., 2007). During activation of place cell input, neurons in the excitatory population are stimulated with an external drive that follows a Gaussian shape with centre given by the position of the simulated animal. The input is periodic and repeats every 10 seconds, with duration of 100 ms. We choose this infrequent update, rather than providing a continuous place cell input that is more likely in vivo, so that the place cell input serves only to correct drift in the position of the attractor bump and therefore we can better test whether the attractor dynamics of the network produce grid firing fields through integration of velocity inputs.

Calculation of connection probability between SCs

We estimate that light drives spiking in a region with dorsal-ventral extent 200 μm, rostral-caudal extent 100 μm and depth 100 μm, giving a volume of at least 0.002 mm^3 (Figure S1 A-C). This is likely an underestimate of the activated volume for several reasons. (i) During light ramps the final irradiance approaches ~15 mW/mm^2 , whereas we evaluated the extent of activation with irradiance of ~10 mW/mm^2. Therefore cells will actually be activated further than 100 μm from the centre of the light stimulus. (ii) Cells are likely to be activated substantially deeper than 100 μm into the slice, as at a depth of 100 μm into cortical tissue light intensity is still at 50 % of its value at the surface (Aravanis et al., 2007). (iii) Recordings were made from cells situated deep in the slice (> 80 μm), so estimates of activation would be greater for more superficial cells.

There are approximately 17800 stellate cells in layer II of mouse MEC (Gatome et al., 2010) and the approximate total volume of layer II is 0.16 mm^3 (~2000 μm dorsal-ventral axis x ~100 μm superficial-deep axis x ~800 μm medial-lateral axis). Therefore the density of stellate cells is ~111000 / mm^3. With rounding down this gives ~ 200 cells in the ~ 0.002 mm^3 area activated by light.

We take this conservative estimate that ~200 stellate cells are driven to spike during light ramps in each slice experiment and consider the data from 11 experiments in Figure S4D-G, in which we fail to observe light-driven EPSCs in any recording, giving a total of 2200 tested potential connections. We conservatively round down to 2000 tested potential connections, none of which demonstrate detectable responses.

We then account for possible sampling variability as follows. Let us assume we have

optically tested N potential connections, and none of them generated a synaptic response. We denote the true connection probability as p. We cannot claim that p = 0, as we have not tested all of the potential connections. However we also cannot say that we are 100% sure that p < 1/N, because there is in fact non zero probability that p > 1/N. Instead, we estimate the range of $p \in [0, p_{max}]$, given a confidence interval C, e.g. C = 95% or similar. Thus, we can estimate a posterior probability of p, given that optical stimulation does not evoke synaptic responses from N potential connections tested

$$P(p|N) = \frac{P(N|p)P(p)}{P(N)}$$

As we don't have any prior knowledge about the connection probability P(p) we assume it is uniform, while P(N) is a constant. Therefore P(p | N) is proportional to

$$P(p|N) \propto P(N|p)$$

which is a probability of randomly testing N potential connections and none of them show a synaptic response, given that the actual probability of connection is p. That is a binomial distribution and therefore

$$P(p|N) \propto P(N|p) = \binom{0}{N}(1-p)^N$$

which after normalization reads

$$P(p|N) = (N+1)(1-p)^N$$

This gives us a likelihood of the probability of connection p given N tested potential connections. We can now set a confidence value C and estimate p_{max} that satisfies $P(p \leq p_{max}) = C$.

$$P(p \leq p_{max}) = \int_0^{p_{max}} dpP(p|N) = 1 - (1 - p_{max})^{N+1}$$

Therefore

$$p_{max} = 1 - \sqrt[N+1]{1 - C}$$

We can then say that with confidence C the connection probability will be less than p_{max}. Therefore, with 2000 tested potential connections and 95% confidence, $p \leq 1.5 \times 10^{-3}$.

Data analysis and statistics

Electrophysiology and simulation data were analyzed using built in and custom routines in IGORpro (Wavemetrics), Matlab (Mathworks) or Python (www.python.org). Excel (Microsoft) and R (www.r-project.org) software were used for statistical calculations. Scalograms were generated using Morlet wavelets and are applied to data filtered with bandpass between 30 and 1500 Hz. Wavelet software was provided by C. Torrence and G. Compo, and is available at http://atoc.colorado.edu/research/wavelets/. Comparisons between groups used ANOVA and Student's t-test as indicated.

To ensure that we restricted our analysis of the relationship between intracellular and local field potential gamma to circuits that were strongly activated, we only included data where the maximum field power exceeded 350 pA^2. For the calculation of the phase of the last spike in the theta cycle only theta cycles with > 1 spike were considered. The phase of the gamma oscillation (Figure 5) is calculated from the Hilbert transform of bandpass filtered reference field potentials. The zero phase of the theta cycle is defined as the middle of the stimulation cycle, where the light intensity is at its highest. The zero phase of the gamma cycle is defined as the trough of the field recording after bandpass filtering in the gamma band. For calculation of spike probability as a function of the phase of optical stimulation we used a bin width of 2 ms.

For analysis of clock-like properties of nested gamma we considered only recordings where the root mean square (RMS) power of the average gamma activity was > 5 times the average RMS of baseline (the first and last eighth of the theta cycle) activity. To

determine the initial gamma cycle in each theta episode we first found the median time across all theta episodes of the first peak that exceeded 3 standard deviations of the baseline after bandpass filtering between 60 and 100 Hz. We then assigned the zero-phase point on the trace closest to the median time as the first gamma peak. Due to gradual rundown of the photocurrent across multiple theta episodes we aligned initial gamma peaks and the times and theta phase of gamma cycles were calculated relative to the aligned peaks.

Because the variance in gamma power was high in control conditions, for comparisons before and after addition of pharmacological agents we log transformed the data and applied statistical tests to the transformed data. The power reduction factors between different pharmacological conditions we report are calculated from the original data.

For simulations, networks receiving a theta input and velocity modulation of the excitatory cells are considered as the control group. Gridness scores are calculated following previous studies (Sargolini et al., 2006), by taking the spatial autocorrelation of each firing field and rotating in steps of three degrees. For each rotation a Pearson correlation coefficient is calculated with the original autocorrelation. To calculate the gridness score the minimum of values at 60 and 120 degrees rotation are subtracted from the maximum of the values at 30, 90 and 150 degrees rotation.

SUPPLEMENTAL REFERENCES

Aravanis, A.M., Wang, L.P., Zhang, F., Meltzer, L.A., Mogri, M.Z., Schneider, M.B., and Deisseroth, K. (2007). An optical neural interface: in vivo control of rodent motor cortex with integrated fiberoptic and optogenetic technology. J Neural Eng *4*, S143-156.

Arenkiel, B.R., Peca, J., Davison, I.G., Feliciano, C., Deisseroth, K., Augustine, G.J., Ehlers, M.D., and Feng, G. (2007). In vivo light-induced activation of neural circuitry in transgenic mice expressing channelrhodopsin-2. Neuron *54*, 205-218.

Fourcaud-Trocme, N., Hansel, D., van Vreeswijk, C., and Brunel, N. (2003). How spike generation mechanisms determine the neuronal response to fluctuating inputs. J Neurosci *23*, 11628-11640.

Fuhs, M.C., and Touretzky, D.S. (2006). A spin glass model of path integration in rat medial entorhinal cortex. J Neurosci *26*, 4266-4276.

Fyhn, M., Molden, S., Witter, M.P., Moser, E.I., and Moser, M.B. (2004). Spatial representation in the entorhinal cortex. Science *305*, 1258-1264.

Garden, D.L., Dodson, P.D., O'Donnell, C., White, M.D., and Nolan, M.F. (2008). Tuning of synaptic integration in the medial entorhinal cortex to the organization of grid cell firing fields. Neuron *60*, 875-889.

Gatome, C.W., Slomianka, L., Lipp, H.P., and Amrein, I. (2010). Number estimates of neuronal phenotypes in layer II of the medial entorhinal cortex of rat and mouse. Neuroscience *170*, 156-165.

Goodman, D., and Brette, R. (2008). Brian: a simulator for spiking neural networks in python. Front Neuroinform *2*, 5.

Guanella, A., Kiper, D., and Verschure, P. (2007). A model of grid cells based on a twisted torus topology. Int J Neural Syst *17*, 231-240.

Hafting, T., Fyhn, M., Molden, S., Moser, M.B., and Moser, E.I. (2005). Microstructure of a spatial map in the entorhinal cortex. Nature *436*, 801-806.

Jones, R.S., and Buhl, E.H. (1993). Basket-like interneurones in layer II of the entorhinal cortex exhibit a powerful NMDA-mediated synaptic excitation. Neurosci Lett *149*, 35-39.

McNaughton, B.L., Battaglia, F.P., Jensen, O., Moser, E.I., and Moser, M.B. (2006). Path integration and the neural basis of the 'cognitive map'. Nat Rev Neurosci *7*, 663-678.

Pastoll, H., Ramsden, H.L., and Nolan, M.F. (2012a). Intrinsic electrophysiological properties of entorhinal cortex stellate cells and their contribution to grid cell firing fields. Front Neural Circuits *6*, 17.

Pastoll, H., White, M., and Nolan, M. (2012b). Preparation of Parasagittal Slices for the Investigation of Dorsal-ventral Organization of the Rodent Medial Entorhinal Cortex. J Vis Exp.

Sargolini, F., Fyhn, M., Hafting, T., McNaughton, B.L., Witter, M.P., Moser, M.B., and Moser, E.I. (2006). Conjunctive representation of position, direction, and velocity in entorhinal cortex. Science *312*, 758-762.